Evaluation of swelling in patients with distal radius fractures

Towards a 3D-printed patient-specific cast

C.J.H. Rikhof
Master thesis Technical Medicine

March, 2020

UNIVERSITY OF TWENTE.

Rijnstate

EVALUATION OF SWELLING IN PATIENTS WITH DISTAL RADIUS FRACTURES.

Towards a 3D-printed patient-specific cast

General information

Cindy Rikhof
Technical Medicine at University of Twente
Department of trauma surgery at Rijnstate

Graduation committee

Chairman	Prof. dr. ir. C.H. Slump
Technical supervisor	Ir. E.E.G. Hekman
Medical supervisor	Dr. E.J. Hekma
Process supervisor	Drs. P.A. van Katwijk
External member	Dr. ir. W. Olthuis

Colloquium

Date	2 April 2020
Time	14:00 Hour
Place	Online

Preface

My academic experience started in 2012 with the bachelor Human Movement Science. I received my bachelor's degree after three years. I enjoyed the technical subjects and the rehabilitation direction. However, I missed the direct link to the clinic and more technical subjects. Therefore, I switch to the master Technical Medicine. This included the big step of moving from Groningen back to Twente.

Before I was allowed to start with this master, I finished a year of pre-master. I started this year with five other students and together we finished this year. I directly liked the practical part of this study. It was a year full of new experiences and a new environment. After this first year, I choose the direction of Sensing and Stimulation. After two M2 internships, I wanted to gain more experience with segmentation and visualization. My interest was in 3D imaging and the analysis of these images. Therefore, I followed extra courses in the direction of Imaging and Intervention.

In April 2019 I started with my graduation internship at Rijnstate. I looked forward to this internship. After the short internships, I wanted a project with technical challenges and more important a patient study. At Rijnstate I got the opportunity to set up a patient study and conduct and analyse the measurements.

I started this year together with Anne-Jet and Lisa. This allowed us to discuss all the steps on the road and to help each other to fulfill this graduation year. So, Lisa and Anne-Jet thank you for the unforgettable year. Of course, also thank you to all other students, researchers, and surgeons (in training) who helped during this year. A special thank you for my supervisors, Edsko who helped to keep my work on track, advised me during this year and answered all my questions. Prof. Slump thank you for your critical view on my thesis and feedback during the year. Edo thank you for providing me with a lot of opportunities clinically, always ready to answer questions and the opportunity to set up a patient study.

I enjoyed my year at Rijnstate and learned to work hard to achieve a goal and gained more self-confidence. I am looking forward to the future!

Abstract

Background - Distal radius fractures (DRF) are the most common type of fractures. They make up for around 15% of all bone fractures. The conservative treatment entails the immobilization with a splint and a plaster cast. Plaster casts are described as uncomfortable and unhygienic and are associated with complications such as stiff joints, neural damage, cutaneous diseases, and loss of muscle strength. To overcome these complications a 3D-printed patient-specific cast is proposed. The aim of the current study is (1) to evaluate the pressure underneath a forearm cast and (2) to evaluate the contralateral side as an input variable for a 3D model.
Method - (1) Five patients with non-displaced DRF were included in the pressure study. With an inductive force sensor, the pressure was measured during the entire treatment period. In total four pressure sensors and two temperature sensors were used per patient. The increase and decrease of the pressure were determined per day and compared among the patients. A questionnaire was used to evaluate the experience of the patient. (2) Thirty healthy volunteers were included in the bilateral symmetry study. From every participant three optical 3D scans were acquired, two of the right arm and one of the left arm. In this study, two different optical 3D scanners were used. Namely, the EinScan Pro and the Structure sensor. Seven circumference measurements were obtained at different points from each scan. Also, heatmaps from the right-right and right-left comparisons were created and compared.
Results - (1) The pressure measurements showed varying results. Three of the patients showed a decrease in the pressure in the first three days in the distal sensors, subsequently, the pressure stabilizes around a value. The questionnaire showed higher pain scores for patients who dropped out of the study after the first week. (2) The circumference measurements showed a mean error of 0.08 mm (sd: 1.39 mm) for right-right comparison and -0.25 mm (sd: 2.39 mm) for the right-left comparison. The heatmaps showed varied results, on average the deviation is similar between the right-right and right-left comparison. In addition, the EinScan Pro provided superior results compared to the Structure sensor.
Discussion/Conclusion - (1) The first results of the pressure study showed that after three days of wearing a splint the pressure was stabilized. Therefore, this would be the ideal moment to replace the splint. Future research should focus on including more patients and more complicated fractures. (2) The bilateral symmetry study evaluated the symmetry of the forearms. The results showed some similarity between the right and the left arm. In future research, the contralateral side can be used. Especially, if thermoplastic material is used, this can overcome a small error.

Keywords: 3D-printed patient-specific cast, 3D-Scan, Bilateral symmetry, Distal radius fracture, and swelling.

Contents

List of abbreviations

DRF	Distal Radius Fracture
3D	three-dimensional
CT	Computed Tomography
L	Inductor
C	Capacitor
LC	Inductive-capacity
AC	Alternating current
ILT	Incremental Load Test
VAS	Visual Analogue Scale
ICP	Iterative Closed Point
MRI	Magnetic Resonance Imaging
PLA	Polylactic acid

0 Introduction

Distal radius fractures (DRFs) are the most common type of fractures. They make up for around 15% of all bone fractures. [1] The incidence is higher in pediatric and elderly people and has increased over the past few years for all ages. It is implied that this increase is caused by changing lifestyles, such as motor vehicle and E-bike accidents, and staying active and independent of the aged population. [2–4] DRFs can be treated either surgically or conservatively, which depends on the severity and type of injury. Conservative treatment entails the immobilization of the fracture with a mineral splint to allow for swelling of the forearm. This swelling occurs directly after fracturing the forearm. After approximately one week the splint is replaced by a circular cast made of plaster or fiberglass to provide better support [5]. It is assumed that the swelling is decreased after approximately one week and the circular cast is fitted to the changed shape and size of the forearm, to provide the necessary support.

There are complications associated with cast immobilization. Plaster casts are often described as heavy, unhygienic, uncomfortable, and poorly ventilated. Depending on the duration of immobilization, complications such as; compartment syndrome, cutaneous diseases, infection, joint stiffness, malunion, neural damage, and loss of muscle strength and function can occur. In contrast, it is often assumed that cast immobilization is without major risk. [6] Furthermore, the time interval between the splint and the application of the final circular cast has not yet been reported in the literature.

To prevent the complications of a plaster cast, three-dimensional (3D) printed casts are being investigated. 3D-printing is a rapidly growing additive manufacturing technique. Despite these rapid developments, 3D-printed patient-specific orthoses are not part of standard clinical care for DRFs. Contrary to traditional treatment, it is not feasible to replace 3D-printed casts after one week, since they are currently more expensive than traditional casts. [1] This means that the 3D-printed cast should compensate for the swelling or be applied after the swelling has decreased. To predict the right moment for changing the splint into a 3D-printed cast or compensate for the swelling, the amount of swelling and the course of the swelling needs to be known. [7] Also, input parameters to create a 3D model of the forearm are required. If the 3D-printed cast is applied after the initial swelling has decreased, input parameters without the swelling are required. For these input parameters, the contralateral side could be used. In order for this to work bilateral symmetry between the forearms is required.

For the development of a 3D-printed model that provides support to stimulate union while staying comfortable for the patient, it is important to gain more insight into the pressures underneath casts and the parameters essential for the creation of 3D-printed orthoses. Therefore, it is necessary to evaluate the size and shape of the fractured arm during treatment time to know which requirements are necessary for optimal conventional treatment. Optimal conventional treatment consists of the shortest possible period of immobilization with accurate healing of the fractured bone, without complications. This research aims to investigate the current treatment of DRFs, in terms of pressure and evaluate parameters for a 3D model, with the goal

of 3D-printing patient-specific orthoses as the standard treatment for DRFs in the future. The swelling will be evaluated with the help of pressure sensors underneath the cast and bilateral symmetry is investigated with the help of an optical 3D scanner, to evaluate its value for the creation of 3D-printed orthoses.

Although the degree and course of the swelling and muscle atrophy after trauma are unknown, it is expected that during the first days after trauma the largest amount of swelling occurs. This swelling is caused by the fracture hematoma, which will decrease over time due to the natural processes of the body. It is assumed that after approximately one week the swelling has disappeared. In conventional therapy, the splint will at this point be replaced by a circular cast. It is hypothesized that in the next phase muscle atrophy will occur and thereby a reduction of the circumference of the arm. The largest degree of atrophy likely occurs at the maximum circumference of the muscle belly. This is due to immobilization and being unable to use the muscles of the forearm. Furthermore, with the help of 3D scans of both forearms, the contralateral side can be evaluated as an input parameter for a 3D model of the affected arm.

This thesis is in partial fulfillment of the requirements for the degree of Master of Science in the subject of Technical Medicine. It is composed of two pilot studies, the pressure study and a study into the bilateral symmetry of the forearms. Together it provides more information that should be utilized during the development of a 3D-printed patient-specific cast. This thesis is composed of multiple themed chapters. After this general introduction, the first chapter elaborates on the clinical background about DRFs, followed by a technical explanation of the used pressure sensors and 3D scanner in the second chapter. The third chapter is about considerations prior to the pressure study. The fourth is about the pressure study, in the form of an article. The fifth chapter elaborates on the bilateral symmetry of the forearms, also in the form of an article. Because both studies will be written in an article style, some general information is repeated. The sixth chapter consists of some for future perspectives. Finally, the last chapter will be a conclusion of the work presented. The appendix contains additional results of both studies.

1
Distal radius fracture

A DRF is a fracture in which the distal end of the radius is broken. The radius is the more lateral bone of the two bones in the forearm, at the side of the thumb. Distally it articulates with the scaphoid, lunate, and distal ulna. This is shown in figure 1.1 [8]. DRFs are frequently caused by a fall with an outstretched hand or a trauma from the outside. One of the major risk factors for obtaining a DRF is osteoporosis, a disease where the density and quality of the bones are reduced. This makes the bones more susceptible to break. Occurrence and progression of osteoporosis increase with age. Therefore, DRFs are frequently seen in elderly patients. [4] In addition, the risk of malunion and loss of reduction is increased in patients with osteoporosis. Nevertheless, it does not influence the healing process. [9, 10]

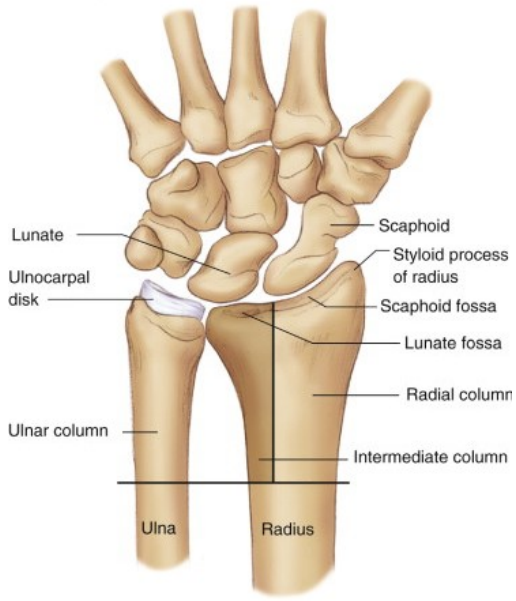

Figure 1.1: Anatomy of the wrist. The distal part of the radius which articulates with the carpal bones can be seen. [8]

There are different types of DRFs based on the position of the fracture and possible displacement of a bone fragment. Studies have shown that the existing classification systems are not reliable. These studies showed that multiple radiologists classify the same fracture differently. This makes a standardized classification

of DRFs difficult. [11–13] The trauma protocol for DRFs of Rijnstate hospital distinguishes the different fractures by using eponyms. The most common type of a DRF, caused by a fall on an outstretched hand, is called Colles' fracture and is characterized by a dorsal tilt. The counterpart is the Smith fracture, also called reverse Colles' fracture. This fracture is characterized by a volar tilt. Furthermore, Barton and reversed Barton fractures can be distinguished. Both are intra-articular fractures in which a radial block is dislocated. For the Barton fracture, the block is dislocated to dorsal and for the reversed Barton fracture the block is dislocated to volar. The final type that is discriminated is a chauffeur's fracture. This fracture occurs through the collision of the distal radius with the scaphoid. It is characterized by an intra-articular impression fracture of the radius and often a fracture of the process styloideus radii. [14]

Research into the additional value of a Computed Tomography (CT) scan to help with the classification of a fracture has indicated that the extra information that a CT scan provides is limited [11]. Therefore, conventional radiography is the first choice method to diagnose DRF. In clinical practice, a CT scan is only indicated in case of consideration of osteosynthesis by difficult fractures. It is important to know the course of a fracture and if it is multifragmentary because the treatment differs between different types of fractures. The examination of a correct position is based on three clinical measurements obtained from x-rays in an anterior-posterior and lateral direction: volar tilt, radial inclination, and radial height. These measurements can be subtracted from an x-ray independent on the settings of the x-ray. Nevertheless, it is important to obtain the x-ray in the right position of the forearm, anterior-posterior and lateral. Values outside the accepted range are an indication of malunion if they are not restored to normal values. Slight differences exist in literature about the normal ranges [15]. These parameters are shown in figure 1.2 and explained below. [3, 16]

A Volar tilt is the amount in which the hand is tilted in volar direction. This is measured in a lateral view, a line along the articular surface and a tangent line are drawn. The normal angle is between 10°-25°, negative volar tilt indicates a dorsal angulation. Extreme dorsal angulation can cause damage to the triangular fibrocartilage complex. This complex consists of ligaments, tendons, and cartilage between the radius and ulna, on the ulna side. This complex stabilizes the wrist.

B The radial inclination is the angle of the distal radial surface with respect to a line perpendicular to the shaft. This is determined by drawing a line from the radial styloid along the articular surface and a line perpendicular to the long axis of the radius. Normally, this angle is 15°- 30°. Abnormal radial inclination can indicate an impaction fracture.

C The radial height is determined by two parallel lines perpendicular to the long axis of the radius. The first line is drawn at the radial styloid and the second line on the articular surface. Normally, this height is between 9.9 - 17.3 mm, with an average of twelve mm. If this height is less than nine mm it is an indication of comminuted or impacted fractures of the distal radius. Shortening of the radial height can cause tears of the triangular fibrocartilage complex and results in a relatively long ulna with respect to the radius. This causes pain in the long-term.

The conventional therapy for DRFs consists of a below-elbow forearm splint for the first week. Before the splint is applied closed reduction under local anesthesia can be used to achieve anatomical alignment of the radius, in case of displaced DRFs. With reduction, the bones are pushed back to their normal anatomical place. Secondary loss of the initial reduction can occur up to two weeks after initial reduction. After the splint, the forearm and wrist are immobilized by a fiberglass circular cast for two to four weeks. Fiberglass is an alternative for plaster, it easier to apply. The duration of the immobilization period is dependent on the severity of the initial fracture. The circular cast is applied in a natural position of the wrist and the metacarpal joints are free. Natural position means slightly dorsal tilt of the wrist. The patient is advised to actively move the fingers and the elbow to avoid stiffness. [13, 14]

Surgical intervention is indicated, if the mentioned criteria are not achieved, despite closed reduction and in unstable fractures. Fractures that are dislocated to volar are by definition unstable, which means operative treatment is required. For patients above 60 years and in young children, the criteria are not as strict as set above. If children are still growing small angulation can grow out of the bone. In elderly patients, the risk of operation should compensate for the limitation of the function. The three major surgical interventions are an external fixator, a plate with screws or Kirshner wires. The external fixator is mainly used in complicated multifragmentary fractures. The fragment needs to be large enough to provide grip for screws in order to

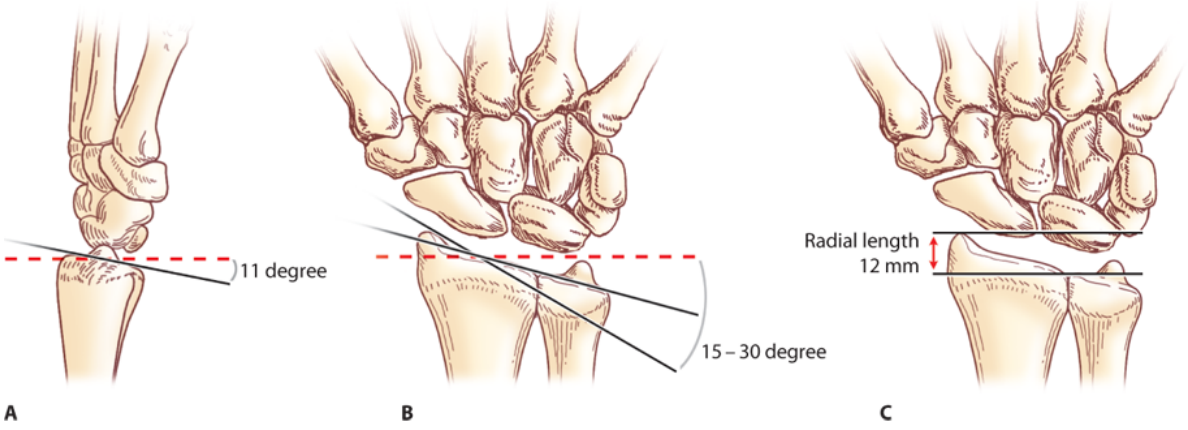

Figure 1.2: Schematic overview of the three different criteria that are assessed in radiographic image to comment on stand. A shows the volar tilt, B the radial inclination, and C the radial height. [16]

apply a plate, which is not always the case in multifragmentary. The external fixator can also be used in a transitional phase in polytrauma situations. In surgery with a plate, the wrist is open reduced and fixed with a plate. Kirshner wires can be used in closed reduction followed by fixation with the wires, this is mostly used in children. Kirshner wires alone are not strong enough for adults. [13, 14]

The goal of all treatment options is anatomical alignment and stability to provide ideal circumstances for fracture healing [17]. Two types of fracture healing can be distinguished: primary (direct) and secondary (indirect) fracture healing. The type of bone healing is determined by the type of treatment. Primary bone healing results from extremely low intra-fragmentary movement. It requires direct bone contact and stable fixation. This is the case in open reduction and internal fixation. There is also no fracture hematoma to initiate the healing because the fracture hematoma is washed away during the operation. Nevertheless, with internal fixation, a stable fixation is achieved. Primary bone healing is based on the direct remodeling of lamellar bone, Haversian canals, and blood vessels. The so-called cutting cones are formed at the fracture site, they consist of osteoclast. They create canals from across the fracture site, which are later filled with bone, formed by osteoblasts. This causes restoration of the Haversian system, which in turn is responsible for revascularization. The bridging osteons are responsible for direct remodeling into lamellar bone without callus forming. [18, 19] In contrast, treatment with plaster cast allows some movement of the bone fragments which is characteristic for secondary bone healing. There are three major overlapping stages in the process of secondary bone healing: inflammation, repair, and remodeling. [17, 20] The literature emphasizes the critical role the first phase plays in bone healing [19, 21]. This first phase is the inflammatory phase and is characterized by a fracture hematoma and inflammation. The fracture hematoma is caused by disruption of the blood vessels during trauma and occurs within minutes after trauma. This disruption of the blood vessels is responsible for the soft tissue swelling and is immediately followed by vasoconstriction and platelet aggregation. This causes hypoxia and low pH environment. The hypoxic condition induces the recruitment of angiogenic factors, which lead to revascularization. The fractured bone region is also invaded by stem cells, mesenchymal cells, and endothelial cells resulting in a hematoma and the formation of granulation tissue. This granulation tissue is a scaffold for the differentiation of osteoprogenitor cells. These cells are osteoblasts and chondrocytes and they lead to the formation of soft callus. The callus formation is driven by chondrocytes. The hard callus is formed during the prolonged remodeling phase, including revascularization and is remodeled into the lamellar bone structure. [17–19, 22]

In conclusion, for non-displaced DRFs the standard treatment is immobilization with a splint and fiberglass cast. This means that in this group fracture healing occurs through secondary bone healing, with a fracture hematoma. This is one of the causes for the swelling. In case of non-displaced DRF, closed reduction is not needed, because non-displaced means that the criteria are in the normal range.

2
Technical background

2.1 pressure sensor

Continuously measurement of the swelling resulting from a DRF is not yet reported in the literature. Therefore it is proposed to measure the pressure between the skin and the cast. This because it is assumed that increased swelling is associated with increased pressure underneath the cast. With pressure sensors, more measurements over time can be taken than with, for example, CT or 3D scans.

The pressure underneath the cast can be measured with the help of pressure sensors. There are different types of pressure sensors commercially available. For example, OEM load cells (Futek Inc., Irvine, CA, USA), force-sensitive resistors (Tekscan, Bosten, MA, USA), and OptoForce sensors (OptoForce, Budapest, Hungary) are pressure sensors. The pressure sensors that will be used in the current study are inductive force sensors, custom made and validated by Giesberts et al. (2018) [23]. They are specially designed for pressure measurements underneath a plaster cast in children with clubfeet. This sensor was designed because the mentioned existing sensors did not meet the set of requirements. The existing sensors were either too bulky or not suitable for long-term precision measurements. The sensor needed to be thin enough to fit underneath a cast without damaging the skin. The power should be supplied by a battery that is safe to use and the measurements should be accurate over a longer period. [23]

An inductive force sensor is based on the fact that the resonance frequency of an inductive-capacity (LC) tank changes when a conductive target is brought in close proximity. An LC-tank is an electric circuit with an inductor (L) and a capacitor (C) in a parallel configuration. An alternating current (AC) is supplied by a small battery into the parallel LC resonant circuit, this generates an AC magnetic field. This magnetic field induces small circulating currents, also called eddy currents, onto the surface of the conductive target. These eddy currents produce an own magnetic field, which counteracts the magnetic field of the inductor. Thereby, the resonance frequency will be changed. The resonance frequency of the LC tank is determined by the inductance and capacitance of the sensors. The frequency follows from equation 2.1. [24]

$$f = \frac{1}{2\pi\sqrt{LC}} \tag{2.1}$$

The inductance to digital converter, LDC1614 (Texas Instruments, Dallas, TX, USA), is used to accurately determine the resonance frequency of the LC-tank. The nominal frequency of the LC-tank is approximately 40 MHz. The nominal frequency is based on an induction of five μH and a capacity of 120 pF. In previous research the resulting pressure ranged from -0.10-2.5 newton [25]. This corresponds with a maximal deviation of 0.375 MHz, based on the sensitivity of 0.15 MHz, subtracted from Giesbert et al. (2018) [23]. To modulate the inductance of a coil, an aluminum target is used as a conductive target. If this target is brought in close proximity of the coil, the eddy current in the target will increase and the inductance of the coil will thereby

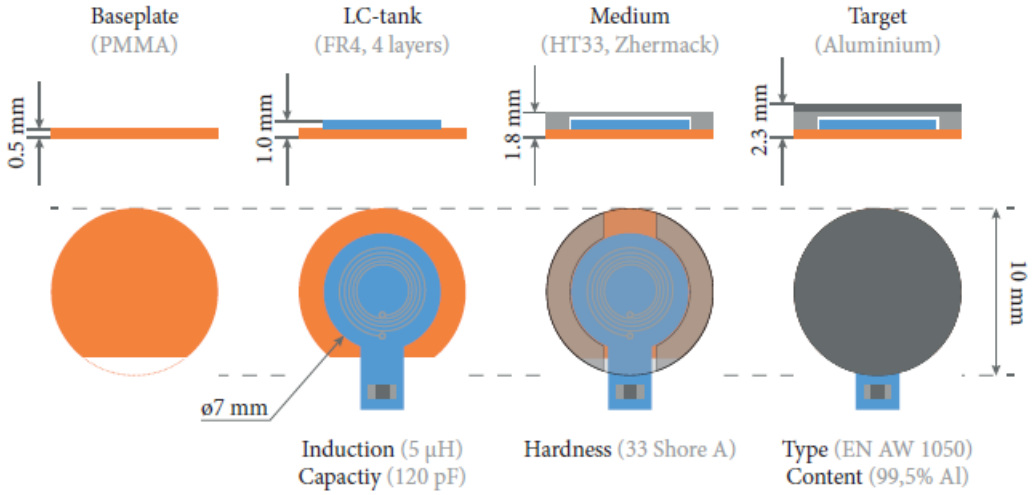

Figure 2.1: Sensor in front and top view in the four different stages of the assembly process.[23]

Table 2.1: Characteristics of the selected inductive force sensor. [23]

Characteristic	**Value**
Dimension (⌀× thickness)	10 × 2.3-2.8 mm
Resolution	0.15 × 10^{-3} N
Accuracy	3.4%
Sample rate	18 Hz
Drift	<2.1 %/log10 (hr)
Hysteresis	6.0 %
Temperature sensitivity	-0.088 N/°C

decrease. To convert this into a force sensor an elastic medium with a known stiffness is added between the coil and the aluminum target. This is shaped into a ring and attached to a baseplate. The different components can be seen in figure 2.1, in a top and front view. The sensor has a diameter of 10 mm and is 2.3-2.8 mm thick. The thickness differs because the thickness of the baseplates is a half mm or one mm. This does not influence the measurements. All the characteristics of the sensor are summarized in table 2.1.

The selected measuring unit contains two inductive force sensors, one temperature sensor, and an acquisition unit. The acquisition unit consists of a control board, battery, sd card reader, inductance to digital converter, and processor (KL25Z). The output of the measurements will be saved on an sd card. A schematic overview is shown in figure 2.2. The temperature sensor is added to correct for the temperature influence on the pressure sensors. The temperature has a negative influence on the measured frequency. Higher temperature causes a decrease in the resonance frequency of the LC-tank, which results in lower measured pressure. The correction value is equal to 0.088 N/°C. Also, it provides information about the temperature induced by applying the cast. [23]

2.2 Structure sensor

In the current study, the Structure Sensor (Occipital Inc, San Francisco, USA) is one of the used sensors to measure the forearm size and shape and to evaluate bilateral symmetry. The sensor is connected to an iPad and uses infrared structured light projection to measure dimensions of the arm. It is a small device that is attached to the back of the iPad. The precision depends on the measuring depth. At 40 cm the precision is approximately 0.5 mm and at a depth of 3 m approximately 30 mm. The field of view is determined by 58

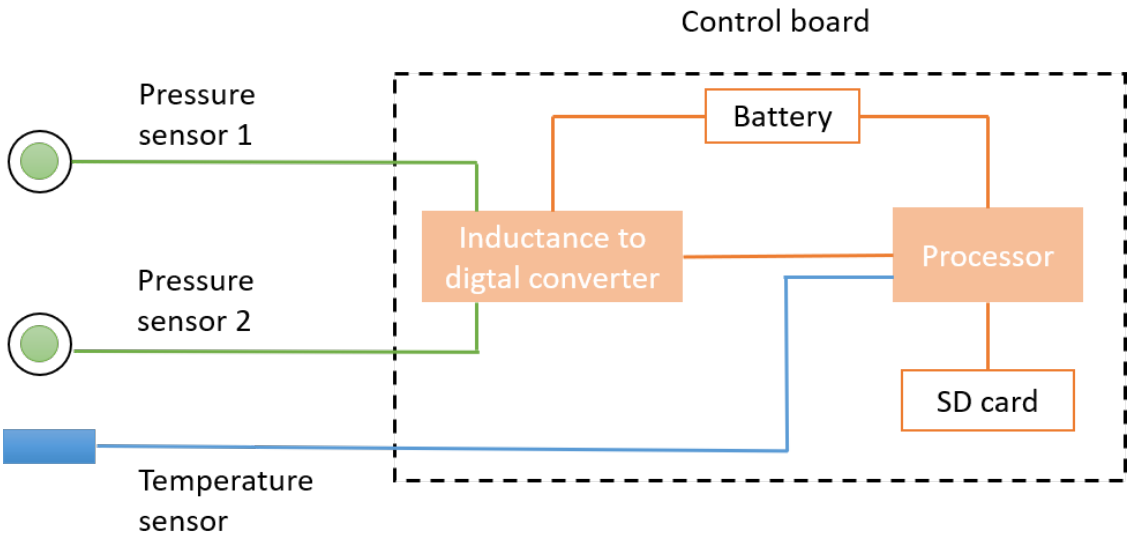

Figure 2.2: Schematic overview of the circuit of the sensor and acquisition unit.

degrees in horizontal direction and 45 degrees in vertical direction, from the center of the sensor. On the left side, the infrared projector is situated and on the right the infrared sensor. To add colors to the obtained image the RGB camera of the iPad can be used. [26]

2.3 EinScan

In the current study a second handheld scanner will be used, the EinScan Pro 2x Plus (Shinning 3D tech. Hangzhou, China). This scanner is also a structured light scanner, with white light. The accuracy of this scanner is 0.1 mm with an additional 0.3 mm per meter. Before the measurements will be conducted, the scanner can be calibrated with a calibration board. It has different scanning options namely: fixed scan, handheld scan, and handheld rapid scan. To add colors a color package can be included. [27]

2.4 Structured Light

From the 3D scans, a 3D mesh is created based on projected structured light. The geometric shape of an arm distorts a 2D image, due to depth differences. Based on this distortion a 3D shape can be extracted. In figure 2.3 an example of a structured light camera is shown. There is one projector which projects, for example infrared, structured light onto the 3D surface of the arm, the illuminated scene is measured with the sensor/camera. Based on equation 2.2, a 3D surface can be calculated. R is the distance between point P and the camera, the depth. B is the baseline, the line between the projector and the camera. θ is the angle between the baseline and the line between point P and the projector. α is the angle between the baseline and the line between point P and the camera. [28]

$$R = B\frac{sin(\theta)}{sin(\alpha + \theta)} \tag{2.2}$$

2.5 Surface comparison

To compare 3D configuration as a whole entity a heatmap can be used. A heatmap is a graphical representation of the data, in which the numeric values are represented with colors. Clinically it is often used to show the differences over time or between patients. In general, green stands for volume increase and red for

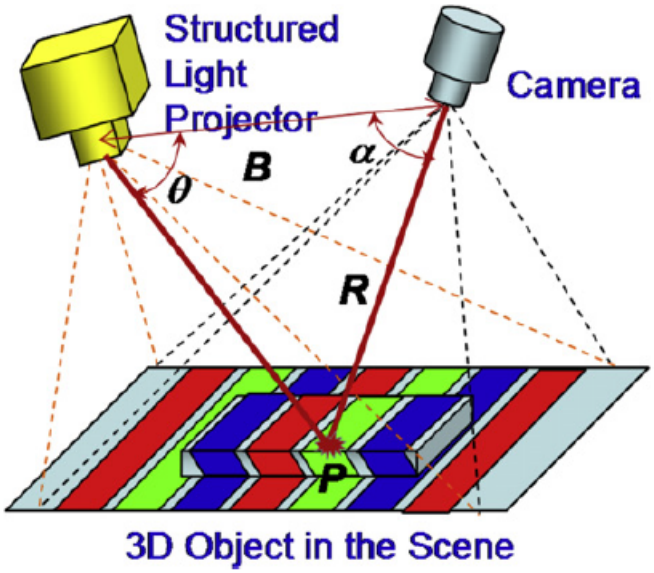

Figure 2.3: Illustration of a structured light-based camera. With B the baseline, R the distance from the camera to point P and θ and α the angles between baseline and point P to respectively the projector and camera. [28]

volume decrease. Heatmaps can be calculated in different ways. Namely, vertex-to-vertex and vertex-to-face distance, which can both be called ray casting. One of the ray casting algorithms is designed by Möller and Trumbore (1997) [29]. This algorithm calculates if and where a ray will intersect with a face. To create a heatmap, one 3D mesh is used as a reference mesh and the other one as the 3D mesh where the rays intersect. [30]

3 Considerations

To measure the pressure underneath the cast, a measurement protocol was designed and the already existing sensors were evaluated and adjusted. In this chapter, some steps of the protocol, adjustments to the protocol, and the sensors are described. Also, test measurements with the pressure sensors were performed on healthy volunteers.

3.1 Requirements sensor

The requirements for the pressure sensor of the study of Giesberts et al. (2018) are equal to the requirements in the current study [23]. Namely, the sensor should be thin enough to fit underneath the cast without damaging the skin, should be accurate enough for measurements over a longer period and the power should be provided by a small battery. A small Lithium-ion-polymer battery (165 mAh) was proposed with the assumption that it should at least measure for one week (168 h). However, for the current study, a longer measurement period is required. The designed sensors were earlier used in research into the correction of clubfeet. In this study, they measured for a shorter period between the battery replacements. The normal treatment requires more visits to the hospital in case of patients with clubfeet, they return weekly. [25] In the pressure study the normal treatment should not be changed, therefore the battery must last for a minimum of three weeks. The amount of energy required for measuring and sleeping mode was unknown. Therefore, the measurement protocol was adjusted until the battery lasted for three weeks. This resulted in a measuring protocol of the first 30 minutes of continuous measurements, followed by 20 s measurements every hour. Continuous measurements will be performed first because the system starts measuring directly after attaching the battery. However, the battery should be attached before the sensors are situated underneath the plaster. To achieve data directly after applying the plaster the sensors measure first continuously.

The pressure study proposes to measure both the swelling due to fracture hematoma as well as the decrease of circumference due to muscle atrophy. Therefore, two acquisition units will be used. One unit will be placed distal at the wrist and one proximal at the forearm. The proximal sensors will be placed on the muscle belly. The flexor muscles form a bulk on the dorsal side of the forearm and the extensor muscles form a bulk at the volar side. It is proposed to place the sensors at these bulks. [31] Distally, the sensors are placed at the radial and volar side. It is expected that this will provide pressure changes in two directions, due to the swelling in these directions. Ideally, the sensors should be placed directly on the skin. However, this gave pressure spots and was not suitable in the patients. Therefore the sensors were placed on the stockinette and the acquisition unit on the outside with pre-tape and/or a layer of fiberglass plaster. The wiring was kept at the radial side, for both acquisition units. In this way, the cast can be removed by cutting or sawing at the ulna side, without damaging the sensors or wires.

3.2 Calibration of the sensors

The pressure and temperature sensor both demand calibration before they can be used. The pressure sensors were calibrated through an Incremental Load Test (ILT). This means that multiple weights were added over time, to determine which resonant frequency belongs to which weight. Subsequently, the weights can be converted into pressure in newton. The calibration method is obtained from Giesberts et al. (2018) and adjusted based on previous studies [23, 32]. Adjustments that were made are designed to save time. To conduct the calibration a wooden framework and a hanger are used, this can be seen in figure 3.1. The calibration started with a zero measurement, for 30 s. Followed by 30 s measurements with the wooden framework and the hanger attached which can hold the weights, with a total weight of 127 g. In the next steps, 200 g of weight was attached and measured for 30 s, between every 30 s measurement 15 s was planned for placement of the weight. In total 1000 g was attached to the wooden framework. This results in seven measurement steps. A schematic overview of the measurement protocol for the calibration of the pressure sensors is shown in table 3.1.

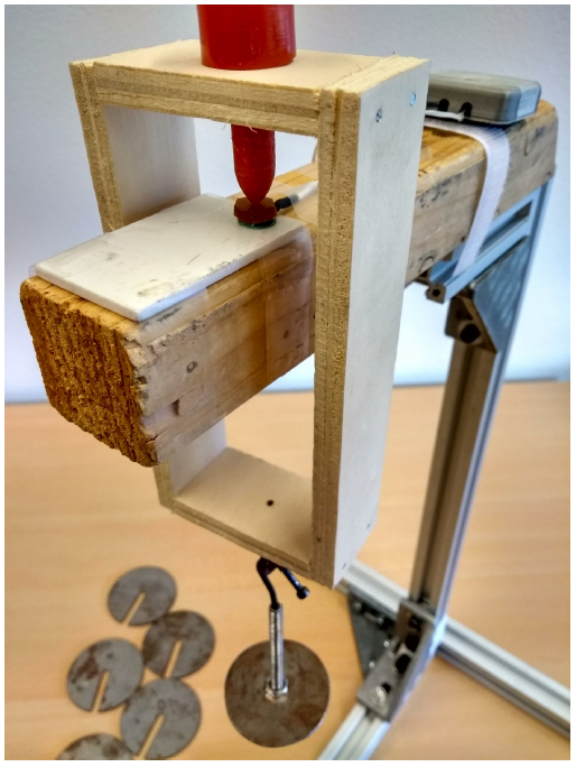

Figure 3.1: Calibration rig, with a wooden framework and hanger. Each sensor was placed in the rig to calibrate. [23]

The calibration of the temperature sensor was conducted to compensate for the offset. The sensors are calibrated at 0.5 °C accuracy at the factory. The compensate for potential offset, the temperature sensors were put on ice water (0 °C) for five minutes. A time-frame of five minutes was chosen because five minutes showed constant measurements and with longer measurements, the same results were obtained. To protect the sensors for water a plastic bag was used, together with a thermometer the sensors were first put in the plastic bag before they were put in ice water.

3.3 Optimization of the sensor

The pressure sensors are handmade. Especially, the medium shaped in a ring was difficult to make. It is a silicone rubber, that was made of two substances. These two substances were mixed, drawn vacuum, and

Table 3.1: Schematic overview of the calibration protocol for the pressure sensors.

Measurement step	Weight (g)	Starttime (s)	Endtime (s)
1	0	0	30
2	127	45	75
3	327	90	120
4	527	135	165
5	727	180	210
6	927	225	255
7	1127	270	300

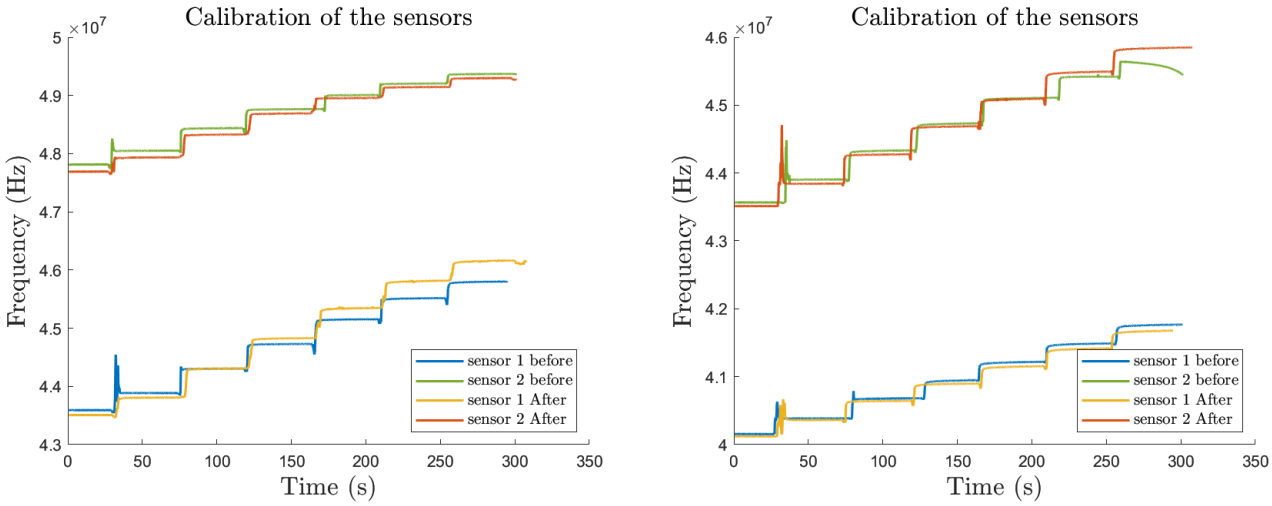

(a) Calibration for the old sensor with silicone rubber ring

(b) Calibration for the new sensor with 3D printed ring

Figure 3.2: Calibration for the different type of ring in the sensors.

injected into a mould, holding five cavities. This mould was drawn vacuum again. After at least four hours of waiting, the mould was opened and five silicone rubbers were extracted from the mould. [33] They were checked on air bubbles because air bubbles make the ring useless, due to an unknown change in stiffness. This custom made design makes the sensors difficult to replicate. To overcome this problem a 3D printed ring was designed and tested. The ring was printed with elastic resin, which is an elastomeric material. This results in a reproducible stiff medium, which is expected to produce reliable measurements.

The 3D-printed ring was first evaluated with a calibration, to determine the range and sensitivity. An example of the calibration before and after a measurement period is shown in figure 3.2. Figure 3.2a shows a calibration for sensor with a silicone rubber ring (old sensor) and figure 3.2b a calibration for sensor with 3D-printed ring (new sensor). The results from the calibration of the old sensors show drift within one sensor. Every step in the calibration, except for the first step, 200 g is added. Ideally, the resulting steps in the frequency are proportional. This means that the increase of the frequency in the second step should be equal to the increase in the third step, etc. This is approximately the case in the new 3D printed ring. In addition, multiple measurements of the same sensor are almost equal to each other. This means that the measurements are repeatable.

3.4 Measurements healthy volunteers

Two healthy volunteers were measured for approximately two hours, with the pressure sensor underneath a fiberglass cast. The sensors measured continuously for these two hours. The volunteers had an age of 23 and 24 years, were left-handed and were both females. The fiberglass cast was applied to the non-dominant hand.

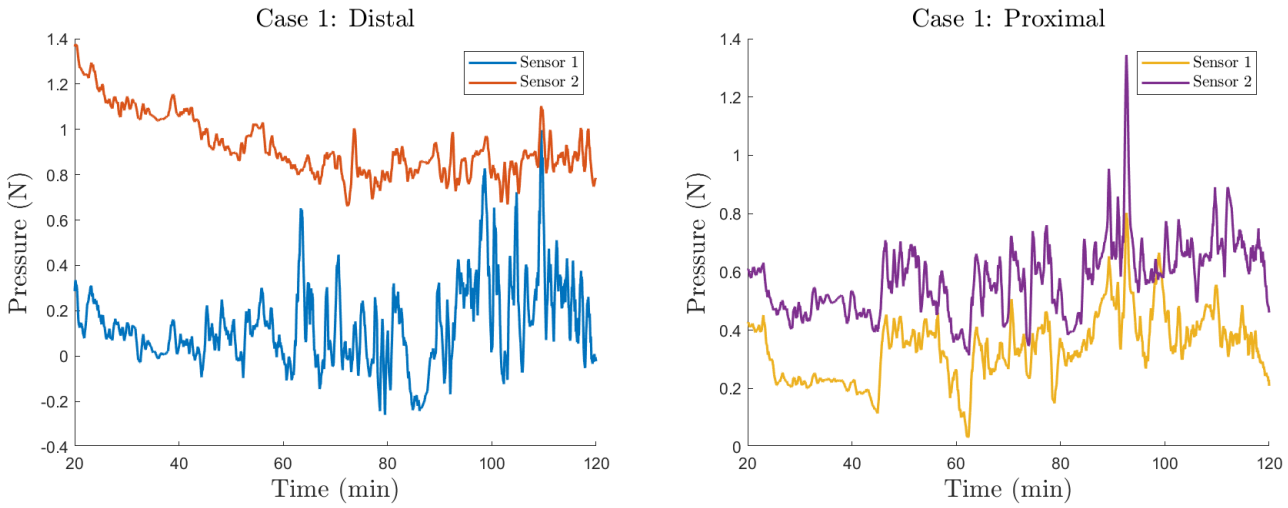

(a) Results of the pressure sensors distal at the forearm.

(b) Results of the pressure sensors proximal at the forearm.

Figure 3.3: Results of the acquisition units distal and proximal of the forearms for case 1.

One had sensors with the 3D-printed ring (case 1) and one with silicone rubber (case 2). The volunteers were instructed to first hold their arm downward, to simulate a kind of swelling, for twenty minutes, followed by holding it upward for ten minutes after that. Thereafter they worked behind a computer for an hour, simulating a normal work environment. After removing the cast and collecting the acquisition unit, another calibration was performed to check if the sensors were not broken down. First, the start and the end of the data were removed, the first twenty minutes and everything after 2 hours after attaching the battery. This to ensure that the visible data is data from underneath the cast and not from applying or removing the fiberglass cast. For the data analysis, a moving average filter with a window of 600 was used. This means that the samples were averaged with the five minutes surrounding the measurement point. Per second, approximately nine measurements are provided. There are not stable measurements, therefore a moving average filter was applied to visualize the increase and decrease over a longer time frame. A period of five minutes was chosen because the tasks had a minimal time frame of ten minutes. Therefore, it is proposed that with a window of 600 samples the increase and decrease due to the tasks can be distinguished.

3.4.1 Results

For case 2 one of the distal sensors broke down, probably while applying the sensor underneath the cast and the whole acquisition unit has stopped measuring. Therefore, only the proximal data of case 2 is evaluated. Figure 3.3 shows the results of the measurements of case 1 for the pressure measurements. The moment of working behind a computer can be distinguished. After approximately one hour there can be seen that the pressure varies more, this indicates more movement. Figure 3.4 shows also a filtered and an unfiltered variant of pressure measurements for case 2. This shows that the moving average filter only removes the noise and the trend can still be observed. Furthermore, figure 3.5 shows the temperature measurements for the different cases. Especially in case one, the moment of starting to use the arm can be distinguished, because the temperature rises after a drop. The same effect can be observed in case 2, but less obvious.

After applying the cast the pressure decreased slightly in most sensors. For the 3D printed ring, most of the pressure measurements are above zero. For case 2 the pressure is close to zero or below zero. Theoretically, this should not be possible because the sensors are calibrated at zero weight. It is expected that the dressing applies a certain amount of pressure, which should result in a pressure above zero at every moment. The reason why the sensors measure pressures below zero is unknown.

These results can help with the interpretation of the data collected by patients with a DRF. They are supposed to hold their arm up for the first week, were after they may use the hand a fraction of the normal usage. The increased fluctuation of the pressure could be an indication of increased use of the hand.

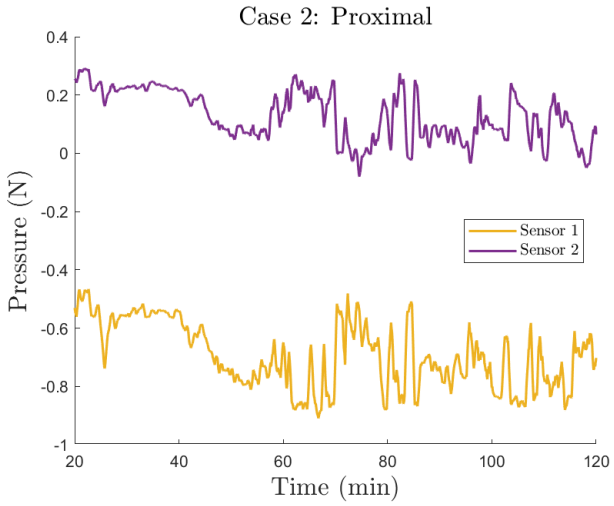

(a) Results of the pressure sensors proximal at the forearm filtered with a moving average filter.

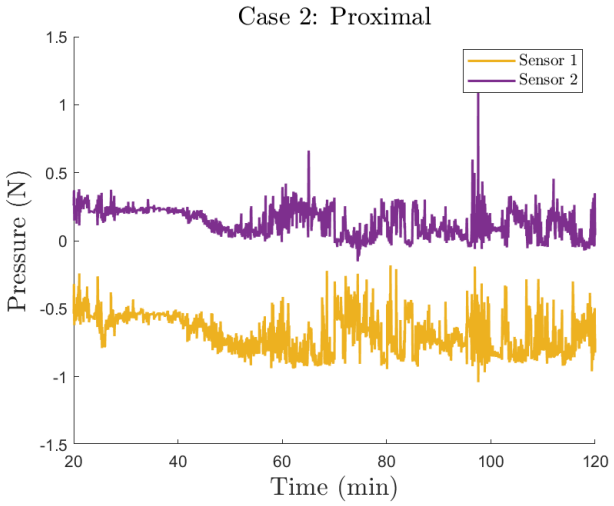

(b) Results of the pressure sensors proximal at the forearm not filtered.

Figure 3.4: Results of the pressure measurements of the proximal unit for case 2.

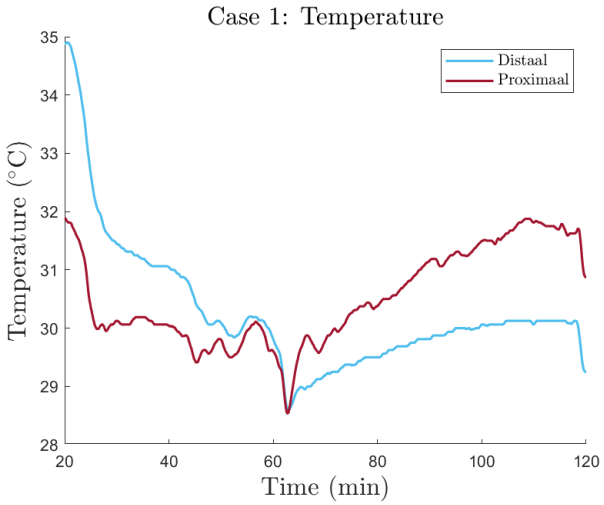

(a) Results of the temperature sensors distal at the forearm for case 1.

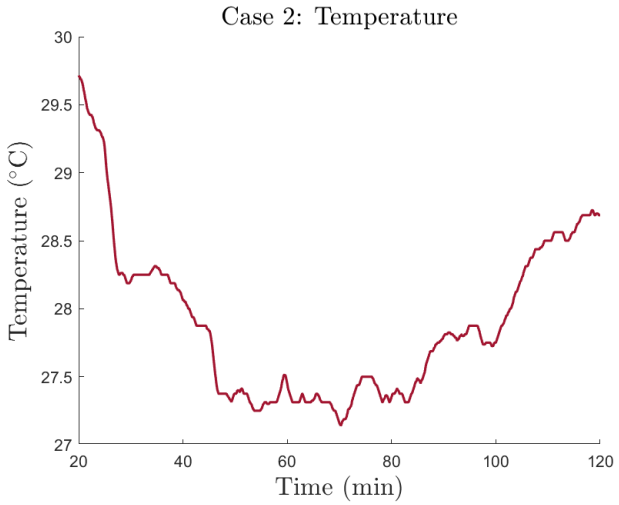

(b) Results of the temperature sensor proximal at the forearm for case 2.

Figure 3.5: Temperature results of the acquisition units distal and proximal of the forearms for the healthy volunteers.

3.5 Recommendations

It is recommended to use the 3D-printed ring to assemble the sensors, instead of the silicone rubber ring. This because it is easier to make and it provides more reliable measurements than the individual made silicone rubber ring. The measurements on healthy volunteers showed measurements above zero with the 3D-printed ring, which is an expected result. The results in patients with a DRF should be evaluated in future research.

Additional optimization of the acquisition unit should be considered. Ideally, the acquisition unit should be smaller and data is stored with bluetooth at an external device. Currently, the data is saved at an SD-card, this requires space in the acquisition unit and the cease of the sensors can not be checked. This can be the case if the data can be checked in real-life.

Also, longer wires should make it easier to apply these sensors underneath the cast and attach the acquisition unit on the outside. To accomplish this the inductance to digital converter should be attached close to the sensor, the length of the wiring from the inductance to digital converter to the control board can be made longer. The length of the wiring between the sensor and the inductance to digital converter determines some characteristics of the sensor. The datasheet for the inductance to digital converter, LDC1614 of Texas Instruments suggest that the wiring between the sensor and the inductance tot digital converter should be as short as possible [24]. Extending the wires will result in another resonance frequency which leads to a measurement error. Figure 3.6 shows a schematic overview of the circuit that will result from placing the inductance to digital converter closer to the sensor and lengthen the wiring to the control board. Also, it is expected that with this configuration more sensors can be attached to one control board. In pairs of two pressure sensors, one temperature sensor, and the inductance to digital converter can be connected to a control board. Ideally, multiple measurements point can be measured with just one acquisition unit.

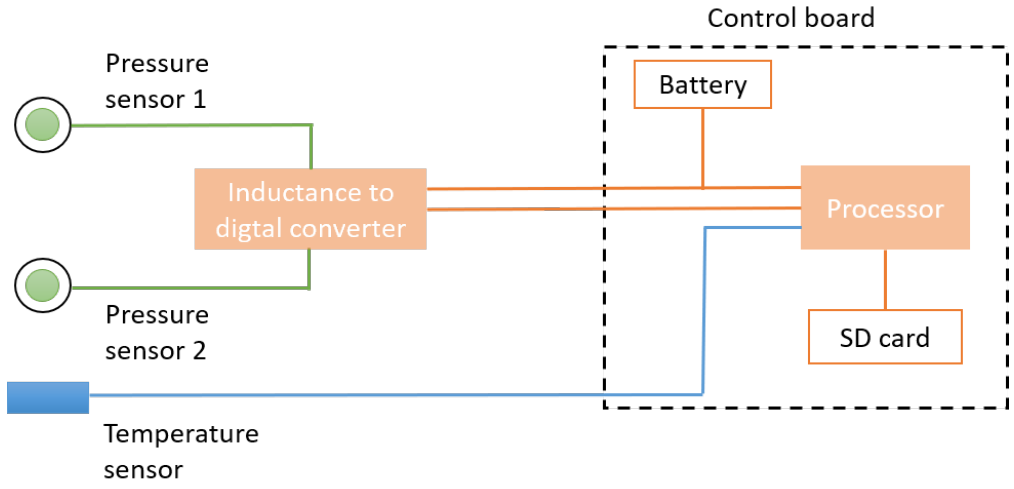

Figure 3.6: Schematic overview of the circuit that results of the proposed changing of the configuration and use longer wires to the control board.

4
Pressure study

Evaluation of the pressure underneath a forearm cast in patients with a non-displaced distal radius fracture

C.J.H. Rikhof, BSc, ir. E.E.G. Hekman, Prof. dr. ir. C.H. Slump, E.J. Hekma, MD.

Abstract

3D-printed patient-specific orthoses are proposed as a new treatment for non-displaced distal radius fractures (DRFs). Before these orthoses can be tested clinically, knowledge about the swelling occurring after fracturing the distal radius is required. The aim of the current study was to evaluate the pressure underneath a plaster cast during conservative treatment. Five patients with non-displaced DRF were included. The pressure was measured at four different points with inductive force sensors. In addition, two temperature sensors were added distal and proximal at the forearm. The measurements showed varying results. Three of the patient had a slight decrease in pressure in the first three days, were after it stabilizes around one value. This means that after three days the splint should be replaced with a 3D-printed patient-specific cast. Future research should focus on including more patients, with adjusted sensors, and clinically testing of the 3D-printed patient-specific cast.

4.1 Introduction

Distal radius fractures (DRFs) are the most common type of fractures. They make up for around 15% of all bone fractures [1]. A large part of these fractures can be treated conservatively, which entails immobilization with a splint and subsequently a circular cast. However, there are complications and discomfort associated with cast immobilization. Complications that can occur are compartment syndrome, cutaneous diseases, infection, joint stiffness, malunion, neural damage, and loss of muscle strength and function. [6]

3D-printed patient-specific casts are investigated as an alternative for traditional casts. It is important that the 3D-printed cast provides enough stability and prevents the mentioned complications. Enough stability is reached if the fracture is anatomically aligned and does not move during the immobilization period. It is known that plaster cast or fiberglass cast provides this stability, but it has not yet been investigated how much stiffness is needed to obtain this stability. Nevertheless, they are currently the golden standard to treat non-displaced DRFs. The first week a splint of plaster is applied followed by 3-4 weeks of a circular fiberglass cast. [34] The time interval for applying the circular cast has not been reported in the literature. It is assumed that the swelling is reduced one week after fracturing the forearm and a tighter circular cast can be applied.

One of the aspects that need to be known to create a reliable 3D-printed patient-specific cast is the swelling that originates through fracturing the arm. This swelling is related to increased pressure underneath the cast because casts are rigid and suppose to fixate the fracture. Pressure measurement underneath the cast can provide information about the pressure executed by the cast to immobilize the forearm as well as the change in forearm thickness due to swelling and muscle atrophy. This information can be used to assess conventional therapy, to create a more efficient therapy for the patient and to help in the design of a 3D model. In addition, it can be an indication of pressure related complications.

Previous research has already evaluated the pressure underneath a cast, mostly concerning splitting the cast or different casting materials. [35–37] Previous research frequently was conducted on healthy volunteers, cadaver arms or models. The swelling was often simulated with the help of fluid bags and pressure measured with a pressure transducer connected to these fluid bags. Moir et al. (1991) also measured patients with Colles' fractures [38]. They compared a plaster cast with a functional Aberdeen Colles' brace. They used the Oxford pressure monitor system (Talley Medical Equipment ltd., Romsey UK.), this system consists of separate pressure cells that are connected to a monitor. A disadvantage of this system is that it does not measure automatically, which resulted in a few measurements in this study. Results showed that the interface pressure underneath the brace was higher but did not exceed the safety boundaries. [38] Literature pointed out that a pressure of 32 mmHg under static conditions is thought to occlude the microcirculation and with 60-75 mmHg eventually skin necrosis will occur [37, 38]. Therefore, the value of 32 mmHg is used as a safety boundary. Furthermore, Patrick et al. (1981) performed the same pressure measurement in patients with non-displaced DRFs. Moreover, they also performed fewer measurements. [39]

No recent research has been conducted on the pressure underneath a cast in patients with a DRF. Also, no continuous measurements are conducted over the treatment period. Therefore, the aim of the pressure study was to evaluate the pressure underneath the cast in combination with the experience of patients with a non-displaced DRF. This information can be used in the design of a 3D model for a 3D-printed patient-specific cast. It is expected that the pressure does not exceed the safety boundaries of 32 mmHg pressure. In addition, a decrease in pressure after one week is expected and the pressure will probably stabilize around one value.

4.2 Method

4.2.1 Study population

Five participants with non- or minimally displaced DRF were included in the current study. They had a mean age of 62.4 years (sd: 16.8 years). A minimally displaced fracture was determined with the following criteria: palmar tilt loss $<10°$, radial shortening ≤ 2 mm and intra-articular step <2 mm determined at radiographs. [40] In practice this means that no reposition technique was used and the radiographs were evaluated by a radiologist. Exclusion criteria were: unstable fracture, reposition at the emergency department, need of surgical intervention, age below 18 and unable to follow the whole treatment at Rijnstate. Participants were recruited at the Rijnstate Hospital, which presented at office hours at the emergency department. Informed consent was obtained from every participant and permission was received from the local feasibility committee (LHC) (dutch: locale haalbaarheidscommissie).

4.2.2 Study design

Pressure measurements were obtained with the custom-designed pressure sensor [23]. The pressure sensors were placed at the socket underneath the webril padding. Dependent on the treatment phase a splint or circular cast was applied by a physician. A small box with the control board and the battery were attached on the outside of the splint or cast, attached with a layer of the casting material and pretape. Two acquisition units were used per patient. One was placed distally, at the height of the processes styloideus, and one proximally, at the height of the muscle belly. Every acquisition unit contained two pressure sensors and one temperature sensor. At the distal placement one sensor was placed at the volar side and one at the radial side. This because it is expected that here the swelling will occur and two directions were chosen to be measured. At the proximal placement one sensor was placed at the dorsal side (extensor muscles) and one at the volar side (flexor muscles). It is assumed that muscle atrophy occurs at these places. One temperature sensors were placed in between the two pressure sensors, for both acquisition units. The pressure sensors were temperature sensitive, therefore a temperature sensor was added to the acquisition unit.

The measurements were obtained automatically according to a pre-set protocol. The first 30 minutes were measured continuously, followed by one measurement of 20 seconds every hour. The remaining

time the acquisition unit went to sleeping mode. The battery of the acquisition unit was changed after one week when the splint was changed for a circular plaster cast. Both pressure sensors were calibrated before and after application underneath the plaster cast or splint. Afterwards, calibration was only performed if the pressure sensors did not break down with removing the cast. This happened in six of the total of 32 used sensors. The number 32 is based on eight sensors per participant, four in the first week and four in the second to the fifth week, except for the first patient and the patients who dropped out after one week. For the calibration, a construction was fabricated at which predefined weight could be applied. The temperature sensor was calibrated as well. With this method, the off-set of the temperature sensor was determined.

Next to the pressure sensors, a questionnaire was filled out twice. Firstly, after one week, concerning the splint and secondly, at the end of the treatment period, concerning the circular cast. This questionnaire was custom made and was focused on the fit, activity level and pain of the patient. The questionnaire was based on the DASH questionnaire and every multiple choice question had a four-point scale. In this way, the patient had to choose between good or bad, because there is no neutral option. Furthermore, some demographic data was collected.

4.2.3 Data analysis

From the pressure measurements, the increase and decrease in pressure over time were visualized. For the measured resonance frequencies, the corresponding pressures were determined with the help of the calibration measurements. The temperature of the measurement and the calibration measurements were corrected for the off-set of the temperature sensor. In addition, the temperature difference between the temperature during calibration and the temperature during the measurements was determined. Compensation for the temperature offset was conducted before the pressure was corrected for the influence of temperature. With this temperature, the pressure measurements were corrected for the influence of the temperature. A schematic overview of the measurements and analysis is shown in the flowchart below, figure 4.1. The orange box is indicating the resulting pressure underneath the cast.

Every hour, 20 s measurements were collected continuously and eventually translated to pressure in newton. These measurements were averaged, this results in one measurement every hour. Furthermore, a moving average filter was applied with a window of six neighboring points. This means that the values are averaged per quarter day. It is expected that the increase and decrease happen slowly. To investigate this more slow behavior of the pressure a window of six was chosen for the moving average filter. The decrease per day of the pressure was compared between the participants.

Table 4.1: The characteristics of the participants.

Characteristics	**Value**
Participants, n	5
Age, years	62.4 (sd: 16.8)
Gender male:female, n	1:4
Dexterity right:left, n	1:4
BMI	28.53 (sd: 6.3)
Type fracture, n:	
- A2	2
- C1	3

The questionnaire was used to evaluate if an increase in pressure was related to incorrect fitting, more pain, and activity level. Furthermore, it was used to evaluate the experience of the patient for the different casts. This experience was rated with a score between one and four for every question, concerning the fit of the cast. Furthermore, the pain was rated with the Visual Analogue Scale (VAS). A number between zero and ten was chosen, in which zero was no pain and ten the worst pain ever.

4.3 Results

In total five participants were included in the current study from October 2019 until January 2020. Two of the participants only participated in the study in the first week. Also, for one patient the proximal measuring unit was not working during the second week. Table 4.1 shows the characteristics of the participants. Fracture type is indicated following the AO classification system. A2 is a simple extra-articular fracture and C1 is a simple complete articular fracture. Three out of five patients found their health prior to the fracture good, one excellent, and one moderate. One person fractured the dominant side, the other four fractured the non-dominant side. One participant was currently working, the other four were unemployed or retired.

Figure 4.2 shows the results of the pressure measurements underneath the cast for the first week, after applying the moving average filter. Distally, most of the pressure measurements are beneath zero. The calibration before and after were averaged and showed

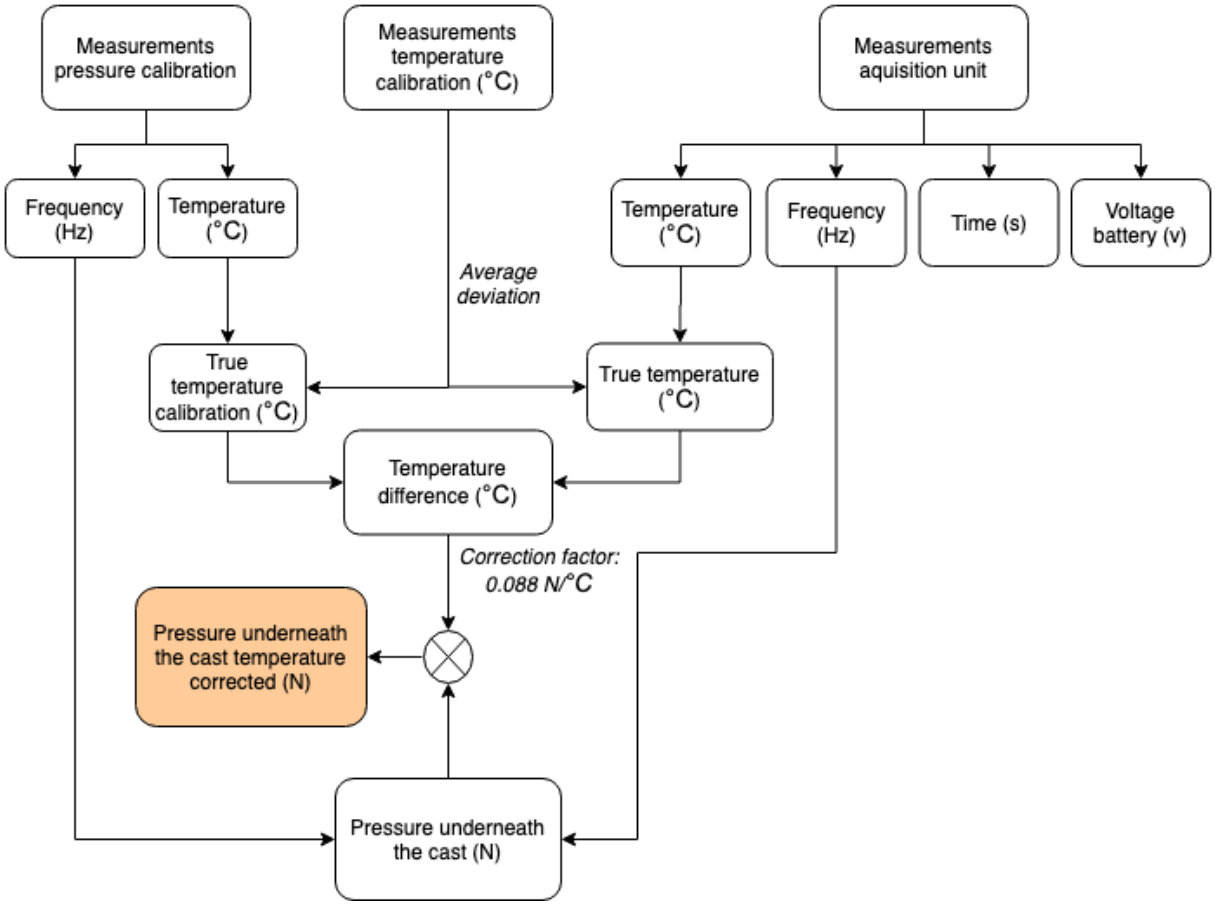

Figure 4.1: Schematic overview of the data analysis of the pressure measurements. The end pressure is given in the orange box.

similar results. The figures show that in the distal sensor the first days mostly a decrease is measured and for the proximal sensor the pressure fluctuates around a value. The decrease of the pressure in the distal sensors stabilizes after approximately three days. Furthermore, it can be seen that the measurement for patient 2 deviates from the measurements of the other patients, except for distal sensor 2 in the first week. In this sensor, the measurement of patient 5 makes a jump in pressure measurements.

Three of the five patients completed the full treatment period with the pressure sensors underneath the cast. The same results were obtained as in the first week. The pressure against time is given in Appendix A, figure A.1. These figures show more stable measurements. Also can be observed that the treatment time with the circular cast differs per patient.

Besides the pressure also the temperature was measured underneath the cast. The temperature measurements are shown in figure 4.3. It can be seen that proximally the temperature is higher, except for participant 2 (P2). In a part of the temperature data, the distal temperature correlates with the proximal temperature. Table 4.2 shows the correlation between the distal and proximal temperature for all participants. There can be observed periodicity in both the pressure signals as the temperature signals.

Table 4.2: Correlation of the distal and proximal temperature measurements.

Patient	**Correlation**	
	Week 1	Week 2
1	0.57	0.53
2	0.48	-
3	0.79	-
4	0.75	-
5	0.78	0.88

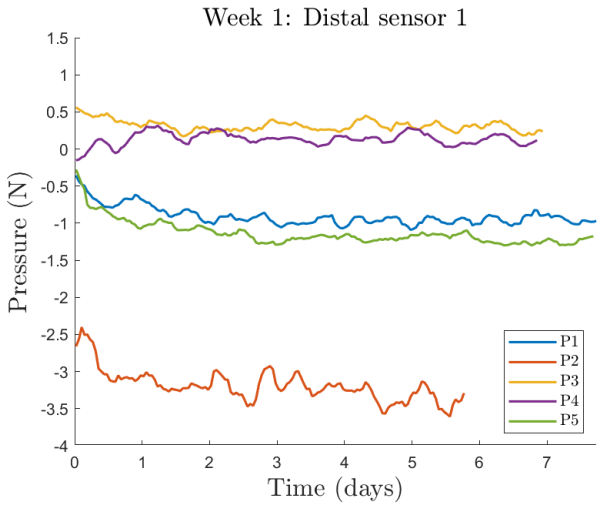

(a) Results of the pressure sensor at the volar side of the wrist.

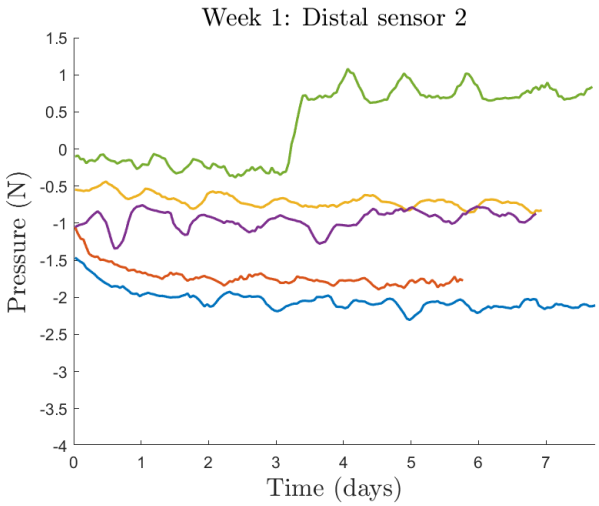

(b) Results of the pressure sensor at the radial side of the wrist.

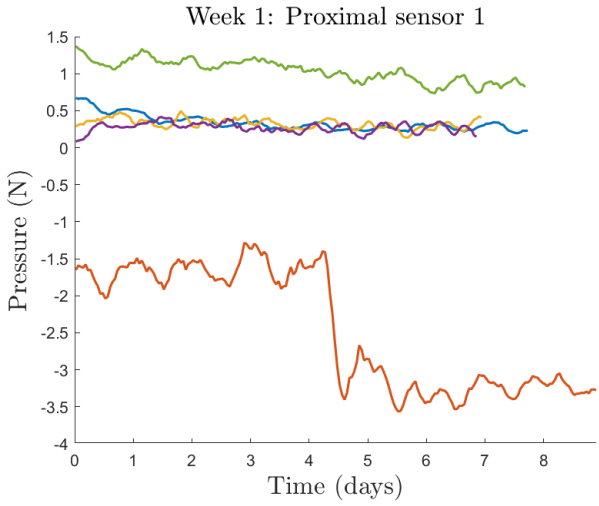

(c) Results of the pressure sensor at the dorsal side of the forearm.

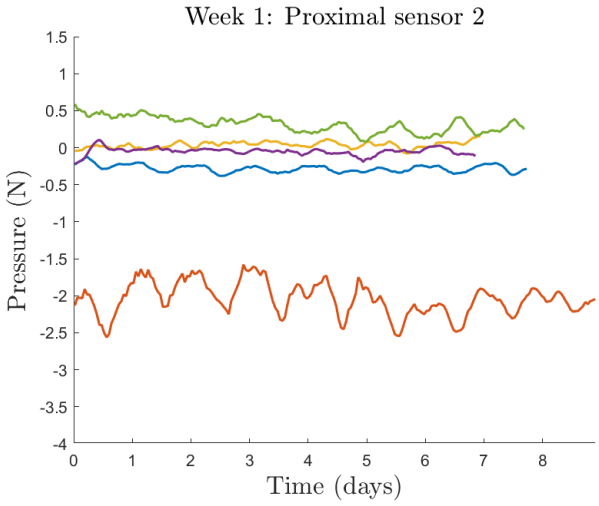

(d) Results of the pressure sensor at the volar side of the forearm.

Figure 4.2: Results of the acquisition units distal and proximal of the forearm. The pressure is shown against the time and the different colors indicate different participants.

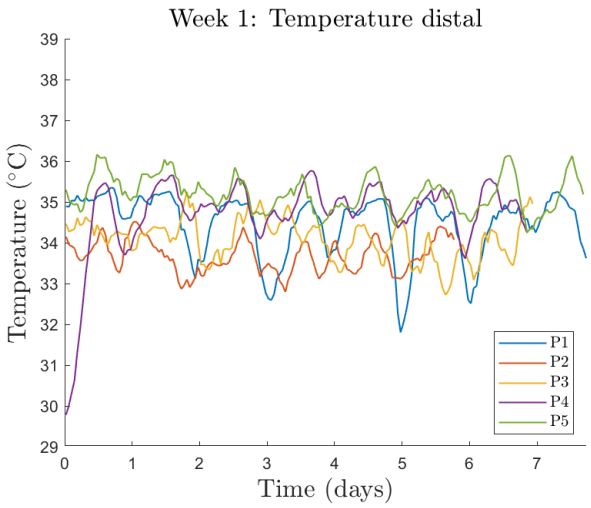

(a) Temperature measurement of the distal acquisition unit.

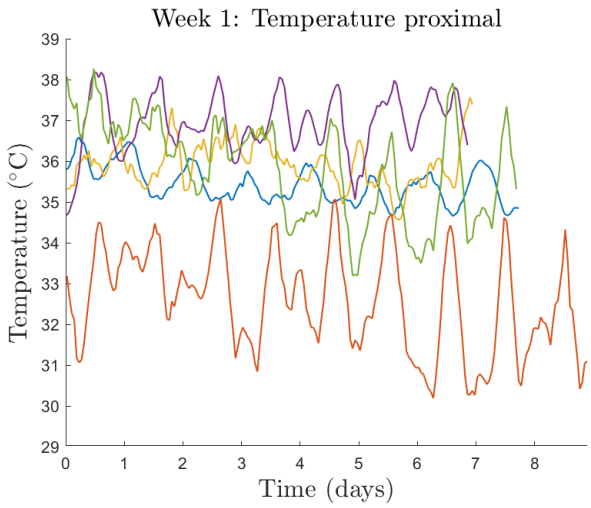

(b) Temperature measurement of the proximal acquisition unit.

Figure 4.3: Results of the Temperature measurement of the acquisition units distal and proximal of the forearm.

Table 4.3: Results of the questionnaire translated to score for the fit of the cast and the pain. A star indicates the use of pain medicine.

	Week 1		**Week 2**	
	Cast	VAS	Cast	VAS
Patient 1	7	0	7	6*
Patient 2	8	3*	8	4*
Patient 3	11	8*	-	-
Patient 4	8	1	7	3
Patient 5	9	5*	-	-

4.3.1 Questionnaire

The experience of the patient about the cast is rated based on the fit, ventilation, and weight. This gives a value between four and sixteen for the variable cast, wherein sixteen indicates the poorest fit and four a good fit. Table 4.3 shows the results of these scores. The patients with the highest pain scores also had more frequent pain and used pain medicine. The use of pain medicine is indicated with a star in the table. In addition, two out of five patients were mildly limited by the cast during daily tasks. The other three were severely limited or impossible to perform daily tasks.

4.4 Discussion

In this study, the pressure and temperature were measured underneath a cast in patients with a non-displaced DRF. Furthermore, the experience and characteristics of the patients were determined with a questionnaire. The results of the pressure measurements show a decrease in the pressure in the first few days after applying the splint for some participants. After the first week, the pressure stays stable in all sensors. The questionnaire indicated that higher pain scores are related to withdrawing after the first week and limited fitting of the cast.

The results of the pressure measurement can not be interpreted as absolute values, because most of the values are below zero and the tightness of the cast can differ. Therefore, the increase and decrease of the pressure are related to the increase or decrease of swelling or muscle atrophy. For the identification of the fracture hematoma, the results of the distal sensors in the first week are important. This showed a slight decrease and fluctuates around a value after three days. This should indicate that after three days the splint can be replaced. The muscle atrophy will likely occur after the first week at the height of the proximal sensors. They showed a stable measurement, this means that there was no measurable muscle atrophy in these participants.

The pressure measurements and the temperature measurements showed a periodicity of approximately 24h. This can be explained with a daily rhythm. At night the arm might be warm underneath a blanket and during the day it might be colder due to the temperature of the environment. Furthermore, the use of pain medication can not be distinguished in the pressure measurements. This means that mild pain medication has no influence on the swelling in a fractured

distal radius in these participants.

To the best of our knowledge, this is the first study measuring the pressure underneath a cast in patients with DRF during the entire treatment period. Patrick et al. (1981) investigated the pressure underneath a forearm cast. They used a pressure probe that was placed over the radial styloid. They did one measurement every hour in the first three hours, followed by one measurement every twelve hours in approximately 72 hours. They only measured the pressure in the first 3 to 4 days, with fewer measurements. [39]

A study that investigated the circumference reduction after immobilization with MRI, found no decrease of the circumference after 21-days of immobilization [41]. This corresponds with the findings in the current study. In the second week, the pressure measured with the proximal sensors fluctuates around one value. This indicates no change in the circumference of the forearm, which suggests the absence of muscle atrophy. This can be due to the low muscle power prior to the fracture. The mostly elderly patients have often already limited muscle strength, which can result in unnoticeable changes with the used pressure sensors.

The strength of this study is the continuous measurement and the use of multiple sensors. In contrast to previous studies, this study measures the pressure at four different locations of the forearm. There is proposed to measure a homogeneous group, to only include fractures that do not need reposition. Nevertheless, the time between the accident and hospital presentation differs but can not be distinguished in the data. With this type of fraction, there is no visible deformation on the outside, which may lead to a delay in hospital presentation.

One of the major limitations of the current study is the number of included patients. Due to strict exclusion criteria, there were a limited number of patients that could be asked to participate. In addition, the main population that fractures their distal radius are elderly people. These patients are more likely to have comorbidities like dementia. In most cases, this population is accompanied by a family member or an attendant and they are more likely to say no, due to the inability to explain the situation to the patient. The study should be continued to include the number of patients determined on forehand. Also, the number of activities that patients perform at home is unknown. This means that it is difficult to explain observed pressure changes.

Another limitation is the variation in the placement of the sensors. The pressure sensors are placed at four different places. Nevertheless, it can only measure the pressure locally at the placed position. After one week the splint was removed and the sensors were switched to new sensors. It was not feasible to leave the sensors because they were placed on the stockinette. The stockinette is also replaced at a plaster change. This results in a variety of placement within one participant and between the participants. In the current study, only the relative values are used. Therefore, the different starting pressure values in the first and from the second week, after replacing the sensors, were not taken into considerations. Furthermore, fourteen of the twenty pressure measurements in the first week are below zero. In future research, there should be investigated if the start value of the pressure sensors underneath the plaster can be taken as zero pressure. The values below zero suggest that besides the temperature environmental factors influence the pressure measurements.

Clinically, this study is the first step toward more knowledge about the swelling in patients with a DRF. To use this information, more patients should be included and ideally, the pressure measurements should be combined with 3D scans of the forearm. In future research, the 3D-printed ring can be used to assemble the inductive force sensor, to obtain reliable measurements.

4.5 Conclusion

A pilot study was performed to measure the pressure underneath a cast, to evaluate the swelling in patients with a DRF. This to determine the appropriate moment to apply a 3D-printed patient-specific cast. The pressure decreases the first days and stabilizes after three days of wearing a splint, this would thereby be the ideal moment to apply a 3D-printed cast. In future research, the swelling should be evaluated in more complicated fractures, children and concerning daily activities that were performed.

5

Bilateral symmetry study

The contralateral side as input variable for a 3D model of the forearm

C.J.H. Rikhof, BSc, ir. E.E.G. Hekman, Prof. dr. ir. C.H. Slump, E.J. Hekma, MD.

Abstract

To overcome complications arising with immobilization of the forearm in patients with a distal radius fracture (DRF), a 3D-printed patient-specific cast is proposed as an alternative. To print such a cast, input variables are needed to create a 3D model. This can be provided with a 3D scan. However, the affected size can be unreliable due to swelling or deformation. Therefore, the current study aims to evaluate the shape of the contralateral unaffected arm as an input variable for a 3D model. To evaluate this, three 3D scans were obtained per participant. Two of the right arm and one of the left arm. In the current study, thirty healthy volunteers were included. Fifteen were measured with the structure scanner and fifteen with the EinScan Pro. The same position of the forearm was ensured with a previously designed framework. The results showed a mean difference for the right-right comparison of 0.08 mm (sd: 1.29 mm) with the EinScan Pro and 0.5 mm (sd: 2.31 mm) with the structure scanner. Furthermore, the right-left comparison showed a difference of -0.25 mm (sd: 2.39 mm) measured with the EinScan Pro. This means that the EinScan Pro is the superior scanner compared to the Structure scanner. Furthermore, there is more deviation in the right-left comparison, however, these differences are small. This can be overcome with thermoplastic material for the 3D-print or padding inside the 3D-print.

5.1 Introduction

Distal radius fractures (DRFs) are the most common type of fractures. They make up for around 15% of all bone fractures [1]. A large part of these fractures can be treated conservatively, which entails immobilization with a splint and subsequently a circular cast. However, complications and discomfort are associated with cast immobilization. Complications that can occur are compartment syndrome, cutaneous diseases, infection, joint stiffness, malunion, neural damage, and loss of muscle strength and function. [6]

It is proposed that with a 3D-printed patient-specific cast the mentioned complications of conventional treatment can be conquered. Nevertheless, with the current technologies 3D-printing of a patient-specific cast is a time consuming and expensive process. [1, 42] The current treatment consists of two different types of casts, a splint and a circular cast. Such a set-up is undesirable for a 3D-printed orthosis, due to the costs. Besides, with the current technologies, the time required for the production is too

long. However, it is still a viable option to apply a 3D-printed orthosis instead of the secondary circular cast. The initial splint is applied to stabilize the fracture and allow for swelling for 7-14 days. After this period the cast is replaced by a circular cast. This could be a 3D-printed orthosis for two to four weeks. [42]

The swelling of soft tissue is caused by the disruption of the blood vessels in the fracture. The disruption of the blood vessels causes a fracture hematoma, which also initiates the healing process. This develops immediately after trauma. [19, 22] In addition, muscle atrophy will occur due to the immobilization of the forearm. This inactivity causes changes in the oxidative metabolism in skeletal muscles. This develops over a longer period after immobilization. [41, 43]

To create a 3D-printed cast, input parameters for a 3D model are needed and a model must be created. The morphology of the forearm is needed to create a patient-specific model. A previous study at Rijnstate investigated the design of brace for the immobilization of a simple Colles' fracture, based on the biomechanical model of these fractures. This study focused on the design of the brace and not the additive manufacturing method or how it could be created patient-specific. [44] Other studies that used 3D-printed orthoses in a more clinical setting often use CT or Magnetic Resonance Imaging (MRI) scans of the forearms. The first clinical trial of 3D-printed orthoses by patients with DRFs was conducted by Chen et al. (2017). They used CT or MRI scans because they had difficulty with 3D scanning the arm. The major complaint was the need to maintain the same position of the forearm, to obtain reliable input data for the 3D scan. The contralateral sides gave a good fit of the resulting orthoses in their study. However, they advise further investigation to evaluate the bilateral symmetry. [1]

Previous research into the symmetry of the forearm focused on the symmetry of the bones and not the symmetry of the surface of the forearm. The contralateral side is frequently used in the planning of corrective osteotomy surgery. This procedure is performed for the restoration of the anatomical alignment of the distal radius. [15] Different procedures have been used to evaluate the bilateral symmetry of the distal radius. Several studies focused on the symmetry of the radial bone obtained from posteroanterior and lateral radiographs, in 2D. These studies showed less variability between left and right than the differences of normal values obtained from a database. This database consists of clinical measurements from radiographs in a normal population [45, 46] In 3D, Vroemen et al. (2012) studied the bilateral symmetry in a whole 3D-configuration of the radius. They found significant differences, in the length and the rotation of the radius bone. [47] Furthermore, Gray et al. (2019) compared clinical measurements of the left and right wrist. They found no significant differences for six different clinical measurements, such as radial height, volar tilt, and radial inclination. [48] Both studies based there measurements on CT images. No symmetry studies of the forearm are published in literature based on 3D-scanning of the forearm.

3D scanning is a relatively new technique compared to CT, MRI, and X-ray. In the past few years, 3D printing and scanning technologies have increased more than ten times. With this technique, the shape, size, and skin-surface can be measured accurately. It is a safe and fast measuring technique. It only takes seconds to capture the data and it is also more comfortable for patients. [49] For the creation of orthoses structured light is a frequently used 3D scanning method [50].

The current study aims to determine if the contralateral side can be used as a representative 3D-model of the affected forearm. The hypothesis is that this will be the case. Previous research is often performed on the bones and not the surface and CT scans were used as the imaging modality [47, 48, 51]. Furthermore, the results are contradicting for the comparison of the left and right forearms. In the current study, the surface of the forearms is scanned with a structured light 3D scanner and compared within one participant. Per participant three scans will be conducted, two of the right arm and one of the left arm. The accuracy of the method is determined by comparing right-right arms; Validity by comparing right-left arms. Furthermore, the study is conducted twice with different scanners and different study populations. 3D scanning is not previously used for evaluation of the bilateral symmetry, therefore it is also unknown which scanner provides the needed accuracy in combination with difficulty of the scanning process.

5.2 Method

5.2.1 Study population

Thirty healthy volunteers were included in the current study, fifteen per scanner. Fifteen patients were included because a previous study showed that twelve patients should be included in a pilot study [52]. This takes into account the drawback of some participants due to failure of scanning process or the analysis. The measurements with the structure scanner were performed in November and December 2019. Furthermore, the measurements with the EinScan Pro were

conducted in February 2020. The study population measured with the structure scanner had a mean age of 24.6 years (sd: 1.8 years), four males and eleven females. The study population measured with the EinScan Pro had a mean age of 26.7 years (sd: 6.7 years), five males and ten females. Informed consent was obtained from every participant. All participants needed to be aged above 18 years, with no relevant comorbidities or pathology of the forearms. The participants were recruited among employees and interns at Rijnstate Hospital.

5.2.2 Study design

3D-scans of the forearms were obtained with the help of the Structure Sensor in combination with the 3DSizeMe iOS app (TechMed, Canada) and the EinScan Pro (MakerPoint, Arnhem). The scanning protocol was equal for both scanners. The scanning protocol entails scanning the right arm twice and the left arm once.

It was important to maintain the same position of the forearm during the multiple scans. Therefore, a previous custom-designed framework was used to ensure the same position of the forearms during the different scans (figure 5.1). This framework consisted of a handle, a U-shaped arm holder with a backplate, a horizontal bar, a vertical bar with a scale, and a bottom plate. This framework was adjusted according to previous findings [53, 54]. With the help of the scale on the vertical bar, the height of the horizontal bar can be read from these centimeters. Participants were instructed to hold the handle and place their upper arm in the u-shaped holder below the handle. The point of the elbow, olecranon, and part of the forearm should touch the backplate The height was adjusted according to the length of the forearm and noted. Additional information was documented, such as age, gender, arm dominance, and physical activity level.

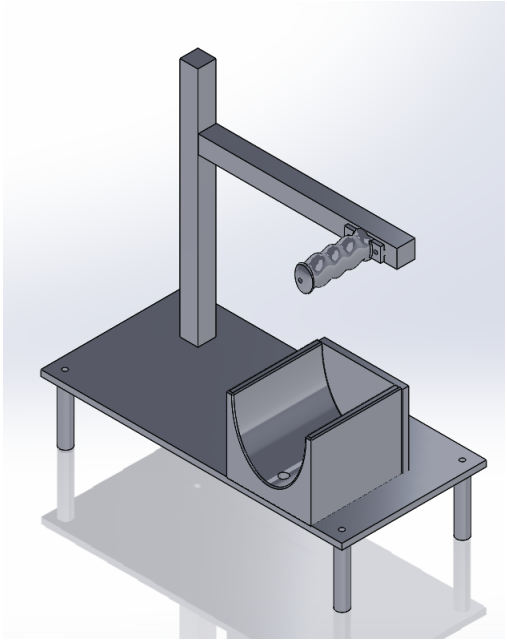

Figure 5.1: Overview of the custom-designed framework with the new adjustments.

5.2.3 Data analysis

For every participant, three 3D-scans were obtained and compared. The two right scans were compared and the left scan was compared with the first right scan. All the 3D scans resulted in 3D meshes which were used for the analysis.

First, the region of interest was selected, this means the framework was removed from the scan by cutting off the top and the bottom. The arm holder was used as a cut off reference at the bottom. At the top transition from the hand into the forearm was used as a cut off reference. This was performed with the MSoft software (TechMed, Canada). Secondly, With the help of MATLAB 2019b (MathWorks, Natick, Massachusetts, U.S.A), an iterative closed point (ICP) algorithm was performed to match two 3D-scans. The meshes were also compressed, to reduce computational time. After matching with ICP, a cut off value was determined and the length of the meshes was adjusted, to obtain meshes with equal length. The cut off value was determined 10 mm below the length of the smallest mesh per participant. This value was used for all three meshes. Thereafter, circumference measurements were extracted from every mesh, at seven different points. These points were based on 20%, 35%, 50%, 65%, 80%, 90%, and 95% of the total length of the mesh. 20% is most proximal (close to the elbow) and 95% is most distal (close to the wrist) point at which the circumference is determined. In addition to these measurements, heatmaps were created with a triangle ray intersection. These heatmaps help to locate and visualize potential deviation and to compare the meshes as whole 3D configuration, instead of specific measurements such as the circumference measurements.

The circumference measurements of both scanners were visualized and analysed with scatter plots and Bland-Altman plots to visualize the agreement between the measurements. For the scatter plots the circumference measurements of the different measurements were visualized against each other. An x=y line was added to provide the ideal situation, in which

Table 5.1: Characteristics of the participants for the surface measurements with the different 3D scanners

Characteristics	**EinScan Pro**	**Value Structure scanner**
Participants, n	15	15
Age, years	24.6 (sd: 1.8)	26.7 (sd: 6.7)
Gender male:female, n	5:10	4:11
Dexterity right:left, n	1:14	3:12
BMI	23.15 (sd: 3.19)	21.67 (sd: 1.68)

the different measurements were equal to each other. Bland-Altman plots are graphs of the mean against the differences between two measurement methods. In the current study, these methods were the right-right arms and the right-left arms. Furthermore, the mean error and limits of agreement were shown as horizontal lines in this graph. The limits of agreement were specified by the mean ± 1.96 times the standard deviation. Before the Bland-Altman analysis, the normal distribution of the differences was checked, since the Bland-Altman analysis assumes a normal distribution of the differences. If all the values lie between the two limits of agreement, the results are statistically relevant. Bland Altman (1985) suggested that in the case of testing a new method against a golden standard, the methods can be used interchangeably if all values lie between these limits of agreement. [55]

5.3 Results

45 scans were successfully obtained, from fifteen different participants per scanner. The participants measured with the Structure scanner are numbered with 1-15 and measured with the EinScan Pro numbered with 16-30. Characteristics of these study populations are shown per scanner in table 5.1.

A first visual impression of the circumference measurements obtained from the 3D scans measured with the EinScan Pro is shown in figure 5.2. Figure 5.2a depicts the measurements from the right-right comparison and figure 5.2b depicts the measurements form the right-left comparison. It can be seen that there is a similarity between the measurements for both the right-right and right-left comparison. All measurements are centered around the x=y line. Slightly more deviation can be observed in the right-left comparison compared to the right-right comparison.

Bland-Altman plots of the measurements with the EinScan Pro are shown in figure 5.3, for both the right-right and right-left comparison. In these figures can also be seen that there is some similarity between all measurements. The right-left measurements show more variability around the mean compared to the right-right measurements. Also, the limits of agreement lie further away for right-left comparison. The mean difference for the comparison of the right arms is equal to 0.08 mm (sd: 1.29 mm) and the difference for the comparison of the right-left arms is equal to -0.25 mm (sd: 2.39 mm).

There are no significant differences in the right-right and right-left differences for gender and arm dominance. On average, the errors are equal to 0.02% and -0.18% of the mean circumference, for respectively right-right comparison and right-left comparison. In addition, for the right-right comparison the errors range from -1.88% - 3.00% of the mean circumference. For the right-left comparison this range is -3.93% - 3.70% of the mean circumference.

Figure 5.4 shows the scatter plot and the Bland-Altman plot for the measurements of the right-right arms obtained with the Structure scanner. The measurements are centered around the x=y line in the scatter plot and around the mean in the Bland-Altman plot. The results show some variation in the measurements. The mean difference is equal to 0.56 mm (sd: 2.31 mm).

For every participant, measured with the EinScan Pro, two heatmaps were created one for the comparison of the two right arms and one for the comparison of the right-left arms. In figure 5.5 the heatmaps of participant two are shown. All the obtained heatmaps can be found in Appendix B. A blue color is indicated by the lowest deviation between the meshes and red is indicated as the highest deviation between the meshes. The color bar shows the corresponding millimeters. The color bar is set from zero to the maximal deviation per participant, for both heatmaps. Consequently, the range for the heatmaps differs per participant. For all participants, it can be seen that there are some deviations in the heatmaps. In general, the right-right and right-left comparisons are similar. The location of the deviation is frequently located at the top or bottom of the heatmap. In addition, in table 5.2 the maximal and average deviation is presented for every participant. Also, the mean and stan-

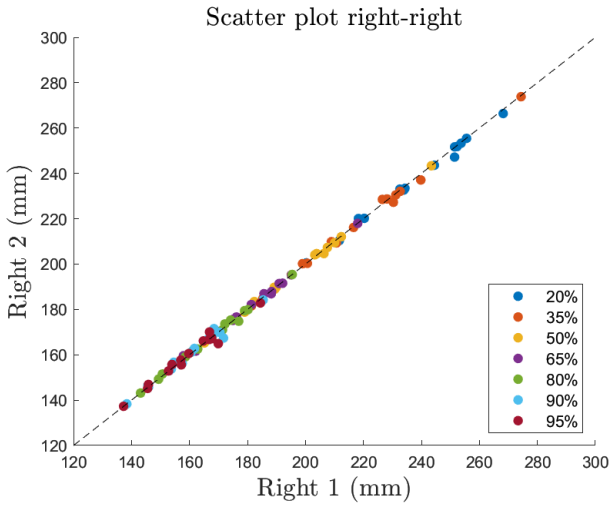

(a) Circumference measurements form the first scan of the right arm against the second scan of the right arm.

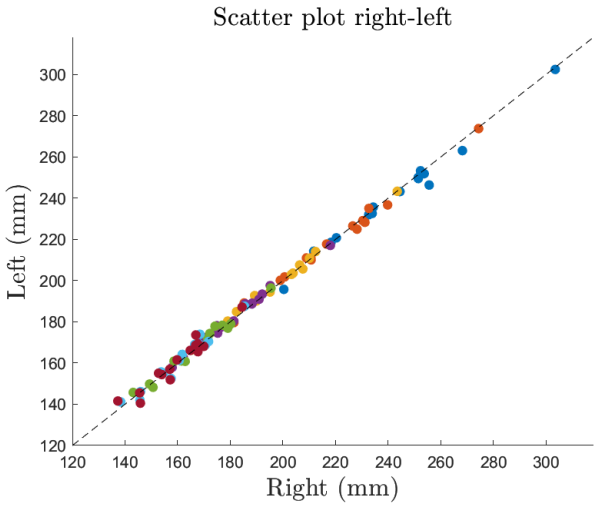

(b) Circumference measurements form the right arm against the left arm

Figure 5.2: Scatter plots of the circumference measurements from the EinScan Pro at different distances of the forearms. The different colors represent the different points at which the circumference is measured. Also, an x=y line is shown with the dotted black line.

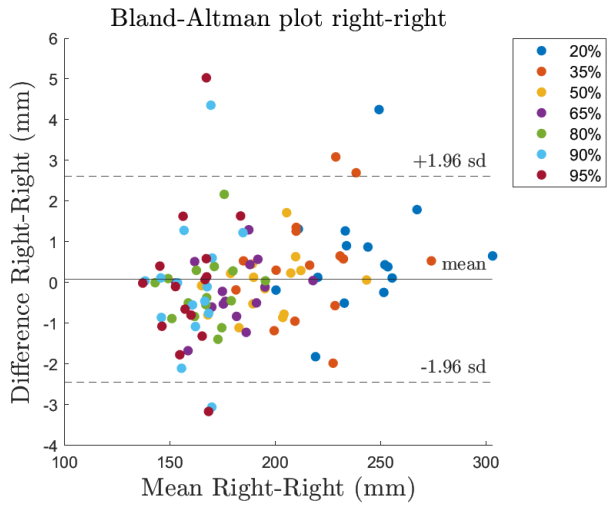

(a) Bland-Altman plot of circumference measurements of the right-right forearms.

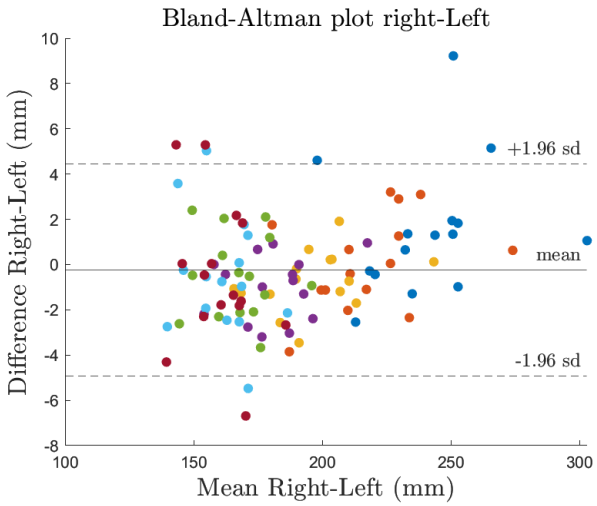

(b) Bland-Altman plot of the circumference measurements of the right-left forearm.

Figure 5.3: Bland-Altman plots of the circumference measurements of the EinScan Pro measurements at different points on the forearms, the different points are indicated with the different colors. The black line indicates the mean difference, the dotted lines indicate the limits of agreement.

dard deviation are provided. The deviations differ per participant. The mean error is mostly lower for the right-right comparison. For the right-right comparison an average maximal error of 2.90 mm (sd: 2.50 mm) was found and for right-left an average maximal error of 4.39 mm (sd: 2.15 mm). The maximal deviation is the ray with the maximal length of the ray-casting method. This method was used to obtain the heatmaps.

5.4 Discussion

The aim of the current study was to evaluate the use of the contralateral forearm as an input value for representative a 3D model. In this study, the left and right arm were compared as whole 3D configurations and with circumference measurements at seven different points. The main results showed some resemblance between the two arms. The found errors

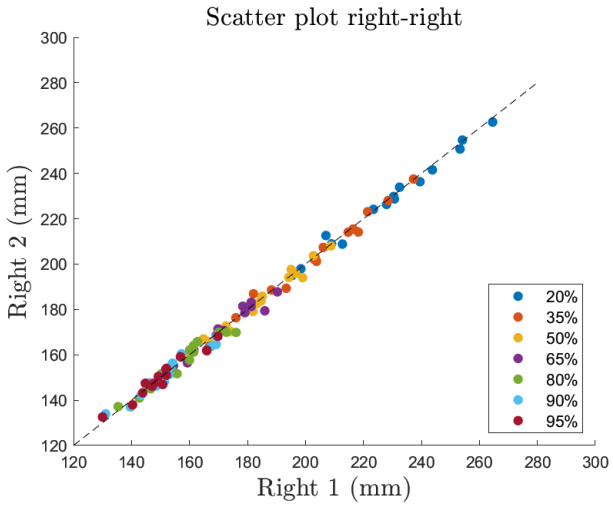

(a) Scatter plot of the right-right comparison with the structure scanner. The dotted line indicates the x=y line.

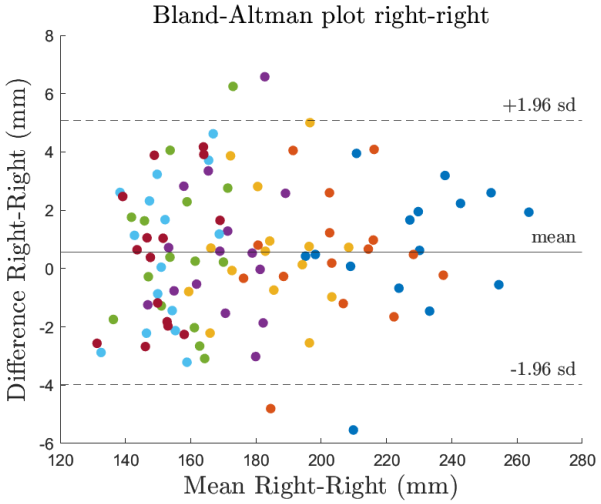

(b) Bland-Altman plot of the circumference measurements of the right-left forearm. The black line indicates the mean difference, the dotted lines indicate the limits of agreement.

Figure 5.4: Scatter plot and Bland-Altman plot of the circumference measurements of the structure scanner at different points on the forearms, the different points are indicated with the different colors.

Table 5.2: The maximal and average deviation in mm of the heatmaps per particpant and the overall mean with standard deviation.

Participant	Right-Right		Right - Left	
	Max	Mean	Max	Mean
16	1.53	0.33	4.10	0.73
17	7.66	0.30	7.89	0.61
18	0.80	0.19	2.00	0.57
19	1.69	0.30	4.85	0.49
20	4.07	0.51	1.63	0.41
21	1.86	0.30	4.93	0.79
22	1.94	0.43	3.57	0.95
23	9.20	0.59	3.20	0.84
24	3.23	0.41	9.64	0.54
25	0.74	0.21	3.75	0.88
26	1.12	0.33	5.76	0.65
27	4.09	0.59	3.18	0.46
28	0.98	0.20	2.20	0.45
29	2.19	0.69	4.09	0.78
30	2.34	0.56	5.11	0.81
Mean	2.90	0.40	4.39	0.66
sd	2.50	0.16	2.15	0.18

between right-left are larger than in the right-right comparison. However, the errors are small compared to the total circumference. In addition, two different scanners were used and the results show superior results of the EinScan Pro compared to the Structure scanner.

The first results of the circumference measurements, the scatter plots, showed slightly more variation in the right-left comparison compared to the right-right comparison. The scatter-plots show also a positive linear relationship. This means that if the measured circumference measurements from one scan increases it also increases in the other two scans. This is as expected because the same measurements were taken. Also, the points lie close to the reference x=y line. Ideally, all the measured points will lie on this line.

For both Bland-Altman plots, not all the values lie within the limits of agreement (dotted lines), which indicates that the circumference measurements of the scans are not totally in agreement. The Bland-Altman plot of the right-left comparison shows also more variability in larger circumferences, in agreement with the results of the scatter-plot. The mean difference of the right-right comparison is in accordance with the proposed accuracy of the EinScan Pro, 0.1 mm. 95% of the data lies between the limits of agreement, this means for the right-right comparison that most of the deviation is smaller than 2.6 mm and of the right-left comparison 4.9 mm. This indicates a small error between the left and right arm.

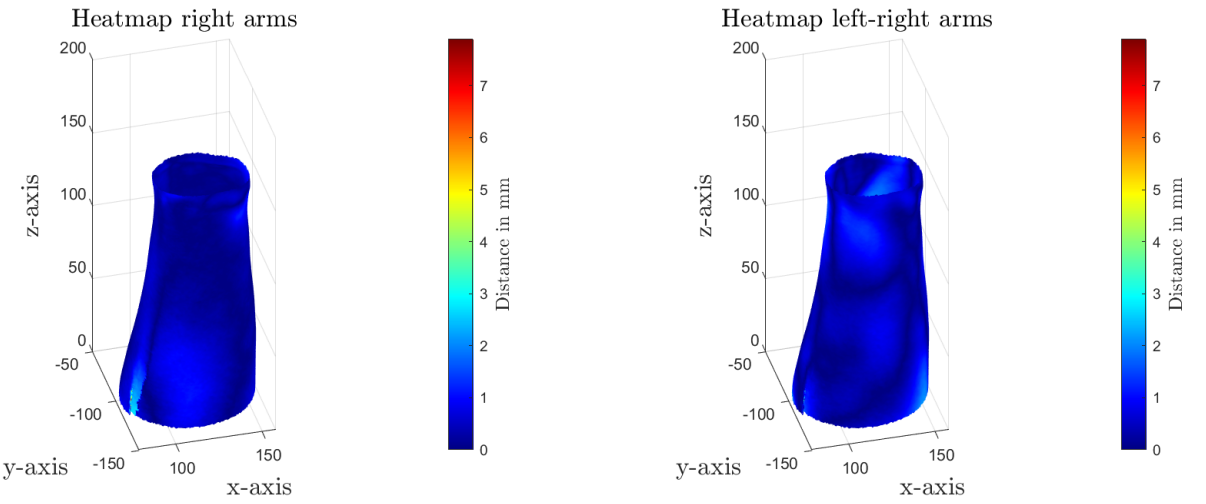

(a) Heatmap of the two scans of the right forearm.

(b) Heatmap of the right and left forearm.

Figure 5.5: Heatmaps of the forearm from participant 2 measured with the EinScan.

In the current study, two different structured light scanners were used. The Structure sensor is easier to use, due to wireless scanning. However, the EinScan Pro is the more accurate scanner of both scanners. This study started with the Structure sensor because for the clinical implementation, easy to use is an important factor. However, the first results showed limited accuracy of the measurements. Therefore, another set of measurements was performed with the EinScan pro. In conclusion, the EinScan Pro is the superior scanner of both scanners in this study. The clinical implication of this scanner should be further investigated.

The results from the heatmap, comparison as whole 3D configuration, show similar results for the right-right heatmaps and the right-left heatmaps. This can be seen in the heatmaps as well as in the provided maximal and average deviation in mm. The maximal deviation provides more information than the mean deviation because an extensive part of the heatmap has a deviation close to zero. This means that the parts that are not in resemblance will be canceled out during averaging. The maximal deviation is the deviation for which a final 3D print should compensate. In most cases, the maximal deviation is at the top or the bottom of the 3D mesh. These are also the interesting parts. DRFs are located close to the top of the 3D mesh, a 3D-printed cast must provide enough support in this region. However, a large part of the deviation is also located proximal of the forearm. These results suggest that in the design of the 3D-model the deviation at the top and the bottom should be taken into account.

The results of the heatmaps are not in resemblance to the study of Vroemen et al. (2012). They found significant differences between left and right when the radius was compared as whole 3D configurations. However, they used CT scans and intensity-based image registration to align part of the 3D configurations of the bones and the mirrored bones. In the current study, 3D scanning is used in combination with ICP registration of the whole forearm, instead of a part of the forearm. The found mean deviations in the heatmaps are small. Therefore, the comparison of the whole 3D configuration can be a beneficial method.

The strength of the current study is that right-right arms are compared to the right-left arms. The found errors can also be due to errors of the scanner or scanning procedure. The current study showed small errors between the right-right comparison, which means that the test-retest reliability is good. However, the found error could be compared to the found error in the left-right comparison. Ideally, the error between the right-right comparison is zero.

The limitation of the current study is the study population. These participants were comparable with each other. However, the population with a DRF are mostly elderly or children. Therefore, in future research, a larger group should be included. In this way the influence of factors like age, BMI, and dexterity should be further investigated. Furthermore, the heatmaps are difficult to interpretable. If there is a large deviation at a particular point, smaller deviations are also visualized with a blue color. This means that a yellow or red color not always means a large deviation. However, if one value was chosen for all heatmaps, also some deviation will not be visualized.

In future research statistical shape modeling can be

considered. With this method, the shape of an object can be described, by applying principal component analysis of landmarks. The use of this method is previously investigated for the use of planning corrective osteotomies and to study the anatomical variance of the distal radius. [56, 57] It is expected that with this method a whole 3D configuration can be predicted. This can also be an option if the contralateral side is not useful through, for example, previous trauma. The residual error of the left-right comparison is equal to 4.9 mm. This is the amount of error a 3D-printed cast should be adjustable for. However, in the process from 3D model to 3D print also an error could be induced. This means that the residual error should be clinically tested. In addition, a thermoplastic material can be fitted in real-life to the forearm of the patient, which can overcome a small error. Furthermore, padding could be added to the design, it could be more comfortable for the patient and overcome a small error.

5.5 Conclusion

The current research investigated the use of the contralateral side. Both methods showed a similarity between the left and right arm. Nevertheless, a small error can be overcome in the model of a 3D-printed cast, if the 3D-printed cast is adjustable. The results of the 3D-printed cast should be tested as well. The EinScan Pro is advised for 3D-scanning of the forearm, due to superior results compared to the Structure sensor.

6
Future perspective

The current thesis elaborates on two pilot studies with the main goal to eventually 3D-print a patients-specific cast for patients with a DRF. Parallel to these studies, the stiffness of a fiberglass cast was determined and a study to translate a 3D scan in a printable 3D model is ongoing.

The stiffness of a cast used in conservative treatment is important to compare to the stiffness of a 3D-printed cast. These 3D-printed casts should provide enough support to stimulate optimal fracture healing. Optimal fracture healing consists of a short as possible immobilization period, with anatomical alignment of the bones and satisfying functional outcome without complications. However, it is unknown if the stiffness provided by conservative treatment is sufficient or excessive. This means that if a model is 3D-printed it can be compared to the found stiffness but, also should be clinically tested. Ideally, a designed 3D-print should prevent stiffness of the joint. This can be overcome to allow some movements that are safe to perform. This will result in faster functional recovery of the wrist.

The material cost of the current conservative treatment is between 5.85 and 11 euro, per cast excluding labor. If there is assumed that both conservative treatment and a 3D-printed cast needs equal manpower, the 3D-printed cast should be around the same cost as conservative treatment. Therefore, laser cutting with polylactic acid (PLA) is evaluated parallel to this study. PLA is a thermoplastic biodegradable material. This means that it can deform with the help of heat. This way the size and holes can be patient-specific but the fitting is created with heating the material. It is expected that this is a faster and cheaper way to create a patient-specific orthosis.

The pressure study provided information about the decrease of swelling after fracturing of the distal radius and applying the cast. Supplementary to determining the swelling for a 3D-model, the information can also be used to optimize the conventional treatment. Currently, a splint is worn for the first week. However, if the swelling reduces after three days the splint can be replaced at this moment. In general, patients experience the circular fiberglass cast as more comfortable than the heavier splint. In some cases, a fiberglass cast is applied directly, if the swelling is limited. The time interval between the splint and the circular cast is expected to be different for more complicated fractures because the fracture hematoma is different.

The results of the bilateral symmetry study showed promising results. Only a small error exists between the right and the left arm. For the 3D-printed model should be determined, which size is necessary to support the fractured arm. Nowadays, the distinction between a below- and an above-elbow cast, is made. A below-elbow cast only immobilizes the wrist. The cast starts approximately two centimeters from the elbow. This means that the elbow can freely move. The length of the forearm cast determines the amount of rotation allowed. A longer cast, in the direction of the elbow, reduces the amount of rotation but has a minor influence on the flexion and extension restriction. [58]

The first step in future research should be including more patients in the pressure study. For the measurements, the sensors with a 3D-printed ring should be used. For the creation of a 3D model the contralateral

side can be used. In future research, the outcomes should be tested clinically. Finally, the 3D-printed patient-specific casts should be designed and clinically tested.

7 Conclusion

This research aimed to evaluate the pressure underneath a forearm cast and to investigate the bilateral symmetry of the forearms. The goal is to create a 3D-printed patient-specific cast for patients with a DRF. The first steps toward a 3D-printed patient-specific cast are made with the current studies.

The pressures were evaluated in a small group of patients with non-displaced distal radius fractures. These first results vary per participant. Distally, some of the patients showed a decrease of pressure in the first three days after applying a splint. Clinically, this should indicate that after three days the splint could be replaced by a circular cast or a 3D-printed cast. Nevertheless, with more complicated fractures this study should be repeated and a different time interval is expected, due to different amounts of swelling.

The contralateral unaffected side can be a valid input parameter for a 3D model of the affected side has too much swelling or deformations. The Einscan Pro is superior to the structure scanner and should, therefore, be the first choice. The remaining error can be overcome with thermoplastic material, in which the 3D-print is fitted in real life to the forearm or with padding material in the 3D-print. The study should be repeated with another study population, the study population should reflect the population with a DRF and a larger study population is needed to investigate the influence of age, BMI, and dexterity.

Bibliography

[1] Y.-J. Chen, H. Lin, X. Zhang, W. Huang, L. Shi, and D. Wang, "Application of 3D-printed and patient-specific cast for the treatment of distal radius fractures: initial experience," *3D Printing in Medicine*, vol. 3, no. 1, p. 11, 2017.

[2] K. W. Nellans, E. Kowalski, and K. C. Chung, "The Epidemiology of Distal Radius Fractures," *Hand Clinics*, vol. 28, pp. 113–125, 5 2012.

[3] J. A. Porrino, E. Maloney, K. Scherer, H. Mulcahy, A. S. Ha, and C. Allan, "Fracture of the distal radius: Epidemiology and premanagement radiographic characterization," *American Journal of Roentgenology*, vol. 203, no. 3, pp. 551–559, 2014.

[4] N. J. MacIntyre and N. Dewan, "Epidemiology of distal radius fractures and factors predicting risk and prognosis," *Journal of Hand Therapy*, vol. 29, no. 2, pp. 136–145, 2016.

[5] J. Petron, David, "Distal radius fractures in adults, Accessed last: 6 March 2020," *Retrieved from: www.UpToDate.com*.

[6] M. Halanski and K. J. Noonan, "Cast and splint immobilization: Complications," *Journal of the American Academy of Orthopeadic Surgeons*, vol. 16, no. 1, pp. 30–40, 2008.

[7] H. Lin, L. Shi, and D. Wang, "A rapid and intelligent designing technique for patient-specific and 3D-printed orthopedic cast," *3D Printing in Medicine*, vol. 2, no. 1, pp. 1–10, 2016.

[8] D. A. Rikli, "Dorsal double plating and combined palmar and dorsal plating for distal radius fractures," *Fractures and Injuries of the Distal Radius and Carpus: The cutting Edge. Philadelphia, PA: Elsevier*, pp. 125–133, 2009.

[9] E. Brogren, M. Petranek, and I. Atroshi, "Cast-treated distal radius fractures: a prospective cohort study of radiological outcomes and their association with impaired calcaneal bone mineral density," *Archives of Orthopaedic and Trauma Surgery*, vol. 135, no. 7, pp. 927–933, 2015.

[10] N. C. Chen and J. B. Jupiter, "Management of distal radial fractures," *Journal of Bone and Joint Surgery - Series A*, vol. 89, no. 9, pp. 2051–2062, 2007.

[11] Y. V. Kleinlugtenbelt, S. R. Groen, S. J. Ham, P. Kloen, R. Haverlag, M. P. Simons, V. A. Scholtes, M. Bhandari, J. C. Goslings, and R. W. Poolman, "Classification systems for distal radius fractures: Does the reliability improve using additional computed tomography?," *Acta Orthopaedica*, vol. 88, no. 6, pp. 681–687, 2017.

[12] D. Wæver, M. L. Madsen, J. H. D. Rölfing, L. C. Borris, M. Henriksen, L. L. Nagel, and R. Thorninger, "Distal radius fractures are difficult to classify," *Injury*, vol. 49, no. June, pp. S29–S32, 2018.

[13] R. Arora, M. Gabl, S. Erhart, G. Schmidle, C. Dallapozza, and M. Lutz, "Aspects of Current Management of Distal Radius Fractures in the Elderly Individuals," *Geriatric Orthopaedic Surgery & Rehabilitation*, vol. 2, no. 5-6, pp. 187–194, 2011.

[14] K. Kolkman and P. Konings, "Traumaprotocol (medisch): Distale radiusfracturen (Rijnstate) (Versie 3)."

[15] G. Caiti, J. G. Dobbe, S. D. Strackee, G. J. Strijkers, and G. J. Streekstra, "Computer-Assisted Techniques in Corrective Distal Radius Osteotomy Procedures," *IEEE Reviews in Biomedical Engineering*, vol. PP, no. c, pp. 1–1, 2019.

[16] S. C. Sherman, *Simon's Emergency Orthopedics*. McGraw Hill Professional, 2018.

[17] L. Claes, S. Recknagel, and A. Ignatius, "Fracture healing under healthy and inflammatory conditions," *Nature Reviews Rheumatology*, vol. 8, no. 3, pp. 133–143, 2012.

[18] R. Marsell and T. A. Einhorn, "The biology of fracture healing," *Injury*, vol. 42, no. 6, pp. 551–555, 2011.

[19] H. Schell, G. N. Duda, A. Peters, S. Tsitsilonis, K. A. Johnson, and K. Schmidt-Bleek, "The haematoma and its role in bone healing," *Journal of Experimental Orthopaedics*, vol. 4, no. 1, p. 5, 2017.

[20] P. Kolar, K. Schmidt-Bleek, H. Schell, T. Gaber, D. Toben, G. Schmidmaier, C. Perka, F. Buttgereit, and G. N. Duda, "The early fracture hematoma and its potential role in fracture healing," *Tissue Engineering - Part B: Reviews*, vol. 16, no. 4, pp. 427–434, 2010.

[21] X. Wang, T. Friis, V. Glatt, R. Crawford, and Y. Xiao, "Structural properties of fracture haematoma: current status and future clinical implications," *Journal of Tissue Engineering and Regenerative Medicine*, vol. 11, no. 10, pp. 2864–2875, 2017.

[22] G. Walters, I. Pountos, and P. V. Giannoudis, "The cytokines and micro-environment of fracture haematoma: Current evidence," *Journal of Tissue Engineering and Regenerative Medicine*, vol. 12, no. 3, pp. e1662–e1677, 2018.

[23] R. B. Giesberts, V. I. Sluiter, and G. J. Verkerke, "Design and test of a new inductive force sensor," *Sensors (Switzerland)*, vol. 18, no. 7, pp. 1–13, 2018.

[24] Texas Instrument, "LDC1612 , LDC1614 Multi-Channel 28-Bit Inductance to Digital Converter (LDC) for," tech. rep., 2014.

[25] R. B. Giesberts, E. E. Hekman, G. J. Verkerke, and P. G. Maathuis, "Rapid decrease of cast-induced forces during the treatment of clubfoot using the Ponseti method," *Bone and Joint Journal*, vol. 100B, no. 12, pp. 1655–1660, 2018.

[26] Occipital, "SDK & Applications - Structure FAQ. Accessed last: 15 March 2020.," *Retrieved from: https://support.structure.io/category/104-sdk-applications.*

[27] Shining, "EinScan Pro 2x Plus - Quick start Guide," tech. rep., 2020.

[28] J. Geng, "Structured-light 3D surface imaging : a tutorial," *Advances in Optics and Photonics*, vol. 3, no. 2, pp. 128–160, 2011.

[29] T. Möller and B. Trumbore, "Fast, Minimum Storage Ray/Triangle intersection," *Journal of graphics tools*, vol. 2, no. 1, pp. 21–28, 1997.

[30] T. Maal, "Mesh Processing and Analysis 3D Computer Vision for Medical Applications," tech. rep., University of Twente and RadboudUMC, 2018.

[31] G. J. Tortora and B. Derrickson, *Principles of Anatomy & Physiology 14th Edition*. 2014.

[32] A. van Elburg, E. Groenendijk, K. Storck, and T. van Zijp, "Multidisciplinaire opdracht - advies over de materiaaleigenschappen van een geprinte orthese bij de alternatieve behandeling van stabiele, niet-verplaatste colles-fracturen," tech. rep., University of Twente, 2018.

[33] Zhermack, "HT 33 TRANSPARENT: Technical Data Sheet 1. Description and Main Features.".

[34] E. A. Delft, T. G. Gelder, R. Vries, J. Vermeulen, and F. W. Bloemers, "Duration of Cast Immobilization in Distal Radial Fractures: A Systematic Review," *Journal of Wrist Surgery*, vol. 1, no. 212, 2019.

[35] C. J. Zaino, M. R. Patel, M. S. Arief, and R. Pivec, "The effectiveness of bivalving, cast spreading, and webril cutting to reduce cast pressure in a fiberglass short arm cast," *Journal of Bone and Joint Surgery - American Volume*, vol. 97, no. 5, pp. 374–380, 2015.

[36] S. Chaudhury, A. Hazlerigg, A. Vusirikala, J. Nguyen, and S. Matthews, "Lower limb intracast pressures generated by different types of immobilisation casts," *World Journal of Orthopaedics*, vol. 8, no. 2, pp. 170–177, 2017.

[37] A. A. Alhandi, N. Lekic, A. A. Patel, E. L. Milne, and L. L. Latta, "Skin Pressure Measurements under a Bivalved Cast stabilized by Utilizing a Knob-Wire system: A Cadaver Model Study," *Texas orthopeadic journal*, vol. 2, no. 1, pp. 39–45, 2016.

[38] J. S. Moir, R. Wytch, G. P. Ashcroft, G. Neil, N. Ross, and D. Wardlaw, "Intracast pressure measurements in Colles' fractures," *Injury*, vol. 22, no. 6, pp. 446–450, 1991.

[39] J. H. Patrick and B. Levack, "A study of pressures beneath forearm plasters," *Injury*, vol. 13, no. 1, pp. 37–41, 1981.

[40] N. Kashmiri, I. A. Shakir, R. R. Akhtar, and R. M. Adnan, "Management of Undisplaced and Minimally Displaced Colles ' Fracture with Thermoplastic Splint Versus Conventional Colles Casting," *Journal of Rawalpindi Medical College*, vol. 20, no. 4, pp. 275–277, 2016.

[41] A. Kitahara, T. Hamaoka, N. Murase, T. Homma, Y. Kurosawa, C. Ueda, T. Nagasawa, S. Ichimura, M. Motobe, K. Yashiro, S. Nakano, and T. Katsumura, "Deterioration of muscle function after 21-day forearm immobilization," *Medicine and Science in Sports and Exercise*, vol. 35, no. 10, pp. 1697–1702, 2003.

[42] A. P. Fitzpatrick, "Design of a Patient Specific, 3D printed Arm Cast," in *The international conference on Design and Technology*, vol. 2, pp. 135–142, KEG, 2017.

[43] M. Motobe, N. Murase, T. Osada, T. Homma, C. Ueda, T. Nagasawa, A. Kitahara, S. Ichimura, Y. Kurosawa, T. Katsumura, A. Hoshika, and T. Hamaoka, "Noninvasive monitoring of deterioration in skeletal muscle function with forearm cast immobilization and the prevention of deterioration," *Dynamic Medicine*, vol. 3, pp. 1–11, 2 2004.

[44] J. ten Brinke, *Development of new brace design for immobilization of distal radius fracture based on a biomechanical model for Colles' type fractures (MSc Thesis)*. University of Twente, 2019.

[45] F. Schuind, S. Alemzadeh, B. Stallenberg, and F. Burny, "Does the normal contralateral wrist provide the best reference for X-ray film measurements of the pathologic wrist?," *Journal of Hand Surgery*, vol. 21, no. 1, pp. 24–30, 1996.

[46] N. Hollevoet, G. Van Maele, P. Van Seymortier, and R. Verdonk, "Comparison of palmar tilt, radial inclination and ulnar variance in left and right wrists," *Journal of Hand Surgery*, vol. 25 B, no. 5, pp. 431–433, 2000.

[47] J. C. Vroemen, J. G. G. Dobbe, R. Jonges, S. D. Strackee, and G. J. Streekstra, "Three-dimensional assessment of bilateral symmetry of the radius and ulna for planning corrective surgeries," *Journal of Hand Surgery*, vol. 37, no. 5, pp. 982–988, 2012.

[48] R. J. Gray, M. Thom, M. Riddle, N. Suh, T. Burkhart, and E. Lalone, "Image-Based Comparison Between the Bilateral Symmetry of the Distal Radii Through Established Measures," *Journal of Hand Surgery*, vol. 44, no. 11, pp. 966–972, 2019.

[49] A. Haleem and M. Javaid, "3D scanning applications in medical field: A literature-based review," *Clinical Epidemiology and Global Health*, vol. 7, pp. 199–210, 6 2019.

[50] P. Volonghi, G. Baronio, and A. Signoroni, "3D scanning and geometry processing techniques for customised hand orthotics: an experimental assessment," *Virtual and Physical Prototyping*, vol. 13, pp. 105–116, 4 2018.

[51] J. G. G. Dobbe, J. C. Vroemen, S. D. Strackee, and G. J. Streekstra, "Corrective distal radius osteotomy: Including bilateral differences in 3-D planning," *Medical and Biological Engineering and Computing*, vol. 51, no. 7, pp. 791–797, 2013.

[52] S. A. Julious, "Sample size of 12 per group rule of thumb for a pilot study," *Pharmaceutical Statistics*, vol. 4, no. 4, pp. 287–291, 2005.

[53] C. J. H. Rikhof, "Design of a framework to stabilize the forearm during 3D scanning in distal radius fractures," *Unpublished report (Clinical rotation Technical Medicine, University of Twente)*, pp. 1–7, 2019.

[54] T. van Helden, "Validation of a low-cost 3D scanner for the assessment of swelling after distal radius fracture," *Unpublished report (Clinical rotation Technical Medicine, University of Twente)*, pp. 0–63, 2019.

[55] M. J. Bland and D. G. Altman, "Statistical methods for assessing agreement between two methods of clinical measurement," *The Lancet*, vol. 327, no. 8476, pp. 307–310, 1986.

[56] S. F. Baumbach, J. Binder, A. Synek, F. G. Mück, Y. Chevalier, E. Euler, G. Langs, and L. Fischer, "Analysis of the three-dimensional anatomical variance of the distal radius using 3D shape models," *BMC Medical Imaging*, vol. 17, no. 1, pp. 1–9, 2017.

[57] L. Vlachopoulos, M. Lüthi, F. Carrillo, C. Gerber, G. Székely, and P. Fürnstahl, "Restoration of the Patient-Specific Anatomy of the Proximal and Distal Parts of the Humerus," *The Journal of Bone and Joint Surgery*, vol. 100, no. 8, p. e50, 2018.

[58] J. K. Kim and E. S. Park, "The effect of short arm cast length on forearm rotation," *Journal of Hand Surgery*, vol. 39, no. 4, pp. 629–633, 2014.

Appendix

Appendix A

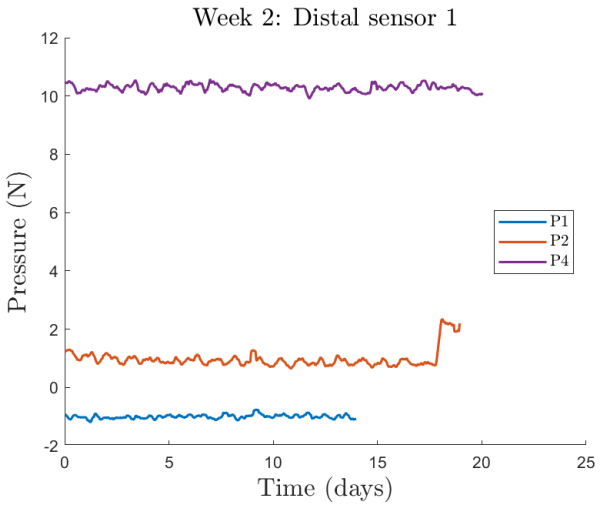

(a) Results of the pressure sensor at the volar side of the wrist.

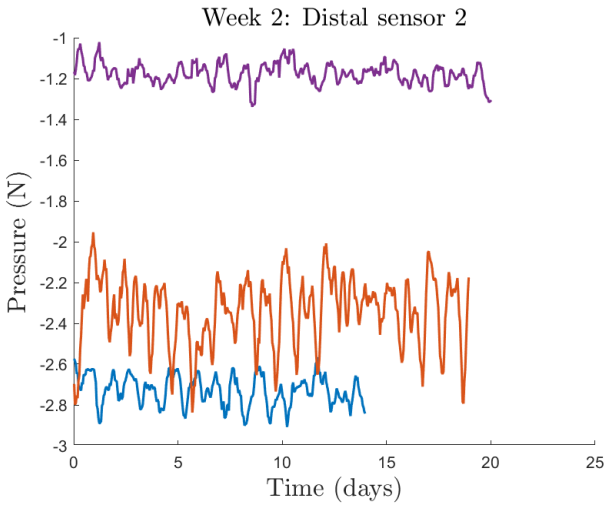

(b) Results of the pressure sensor at the radial side of the wrist.

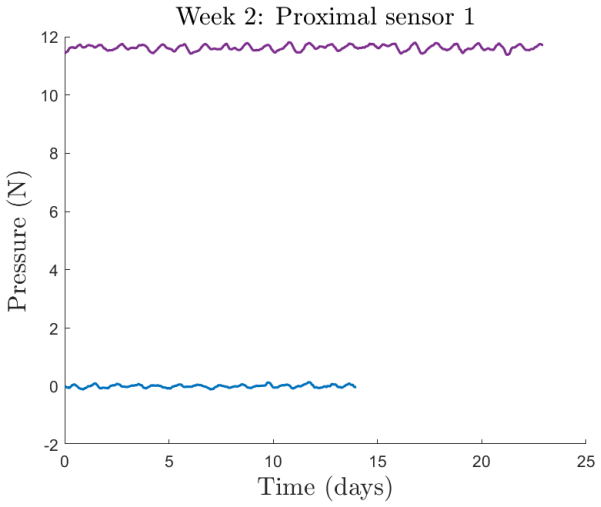

(c) Results of the pressure sensor at the dorsal side of the forearm.

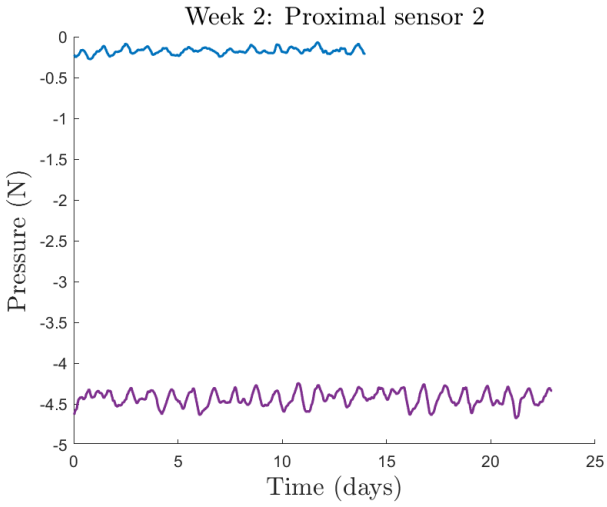

(d) Results of the pressure sensor at the volar side of the forearm.

Figure A.1: Results of the acquisition units distal and proximal of the forearm of the second to third or fourth week.

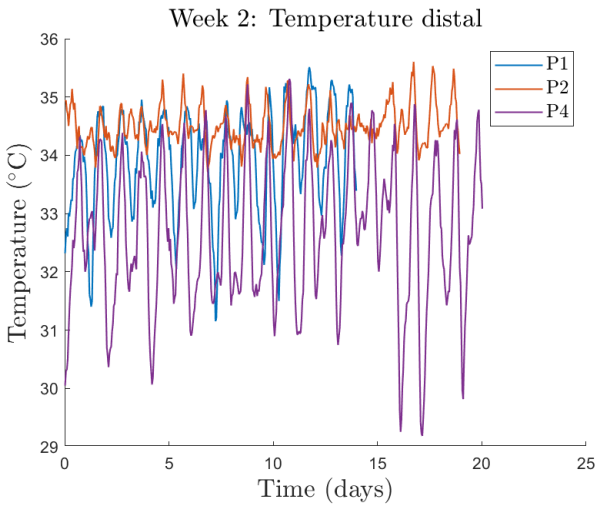

(a) Results of the temperature measurement distal.

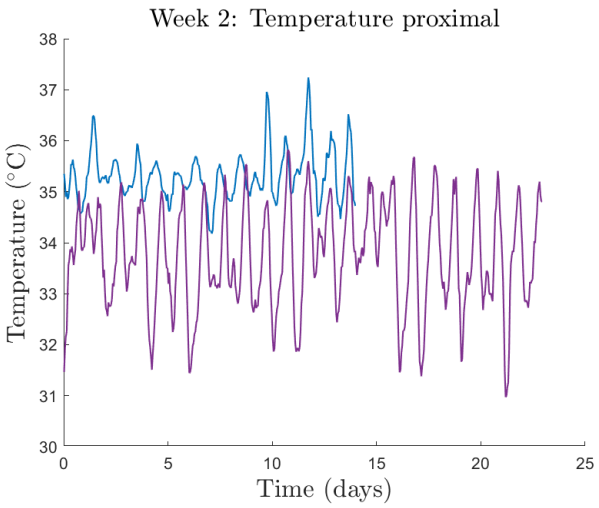

(b) Results of the temperature measurement proximal.

Figure A.2: Results of the temperature measurements distal and proximal of the forearm of the second to third or fourth week.

Appendix B

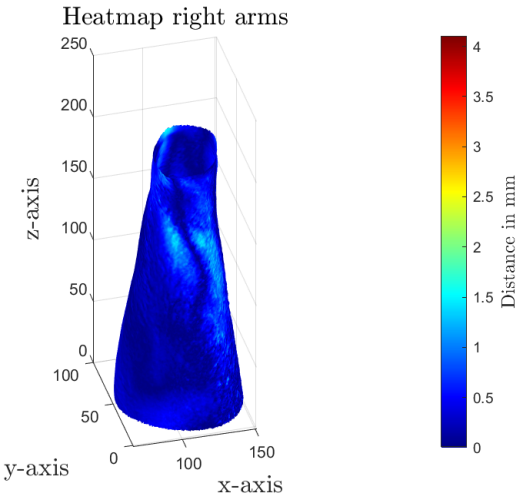

(c) Heatmap of the two scans of the right forearm.

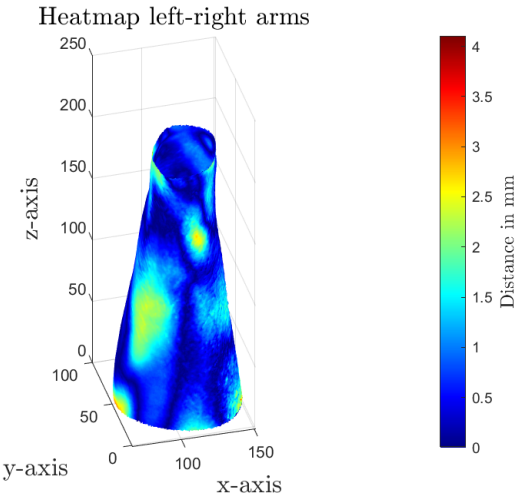

(d) Heatmap of the right and left forearm.

Figure B.1: Heatmaps of the forearm from participant 1.

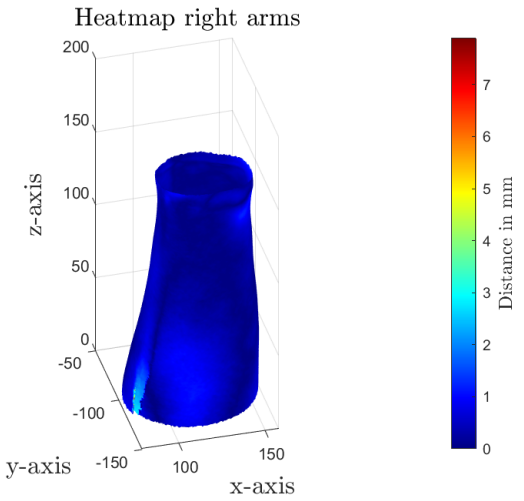

(a) Heatmap of the two scans of the right forearm.

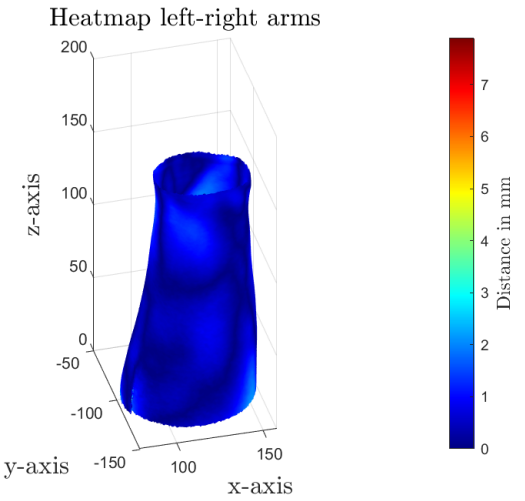

(b) Heatmap of the right and left forearm.

Figure B.2: Heatmaps of the forearm from participant 2.

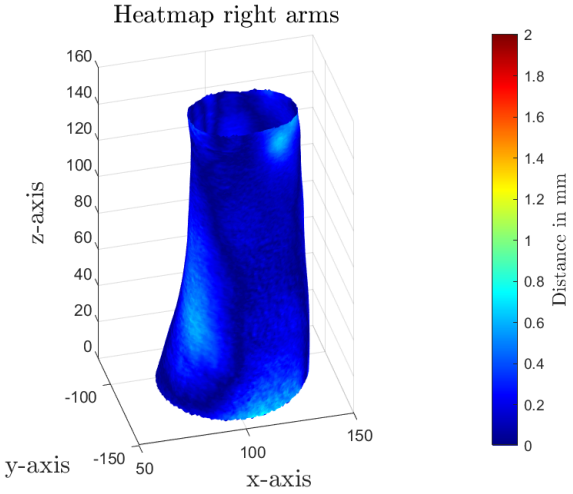

(a) Heatmap of the two scans of the right forearm.

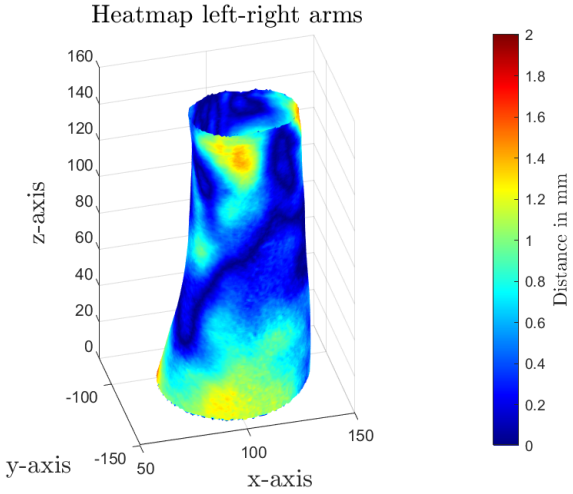

(b) Heatmap of the right and left forearm.

Figure B.3: Heatmaps of the forearm from participant 3.

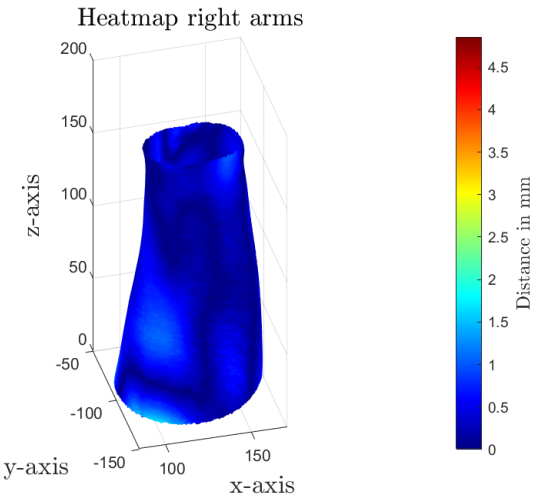

(a) Heatmap of the two scans of the right forearm.

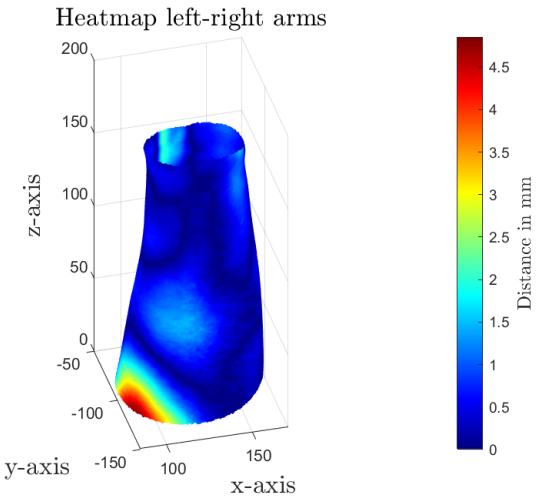

(b) Heatmap of the right and left forearm.

Figure B.4: Heatmaps of the forearm from participant 4.

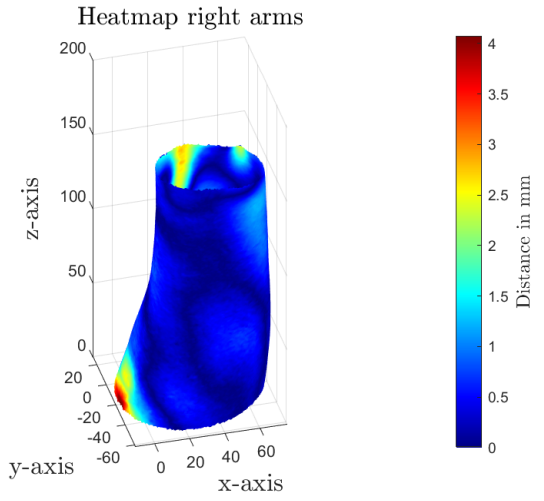

(a) Heatmap of the two scans of the right forearm.

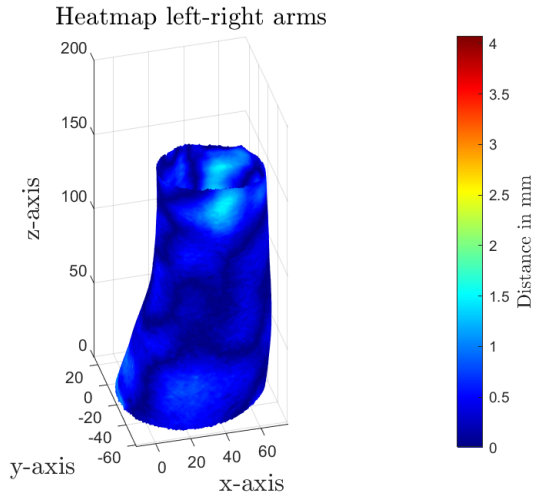

(b) Heatmap of the right and left forearm.

Figure B.5: Heatmaps of the forearm from participant 5.

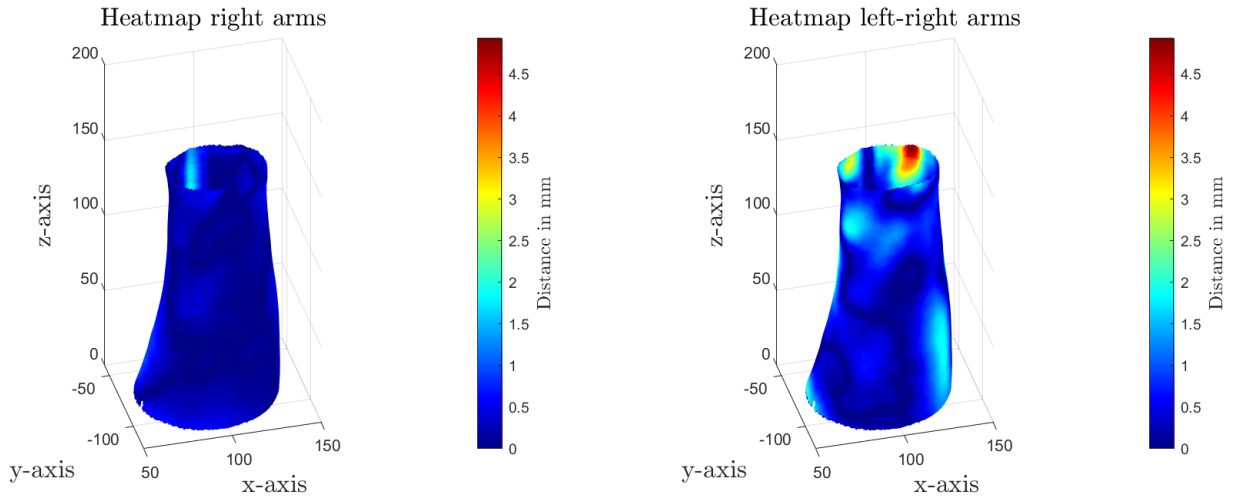

(a) Heatmap of the two scans of the right forearm.

(b) Heatmap of the right and left forearm.

Figure B.6: Heatmaps of the forearm from participant 6.

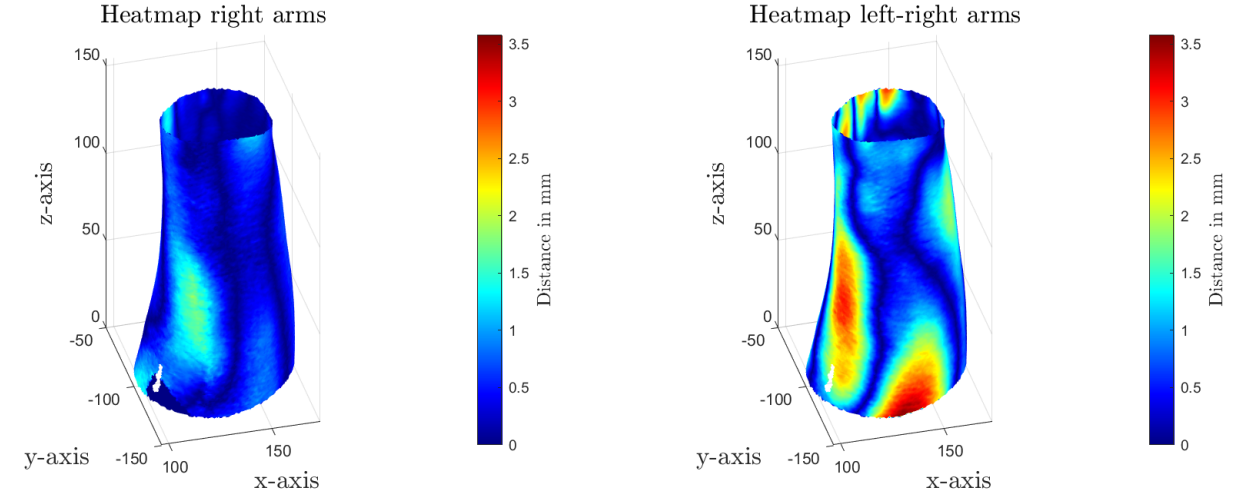

(a) Heatmap of the two scans of the right forearm.

(b) Heatmap of the right and left forearm.

Figure B.7: Heatmaps of the forearm from participant 7.

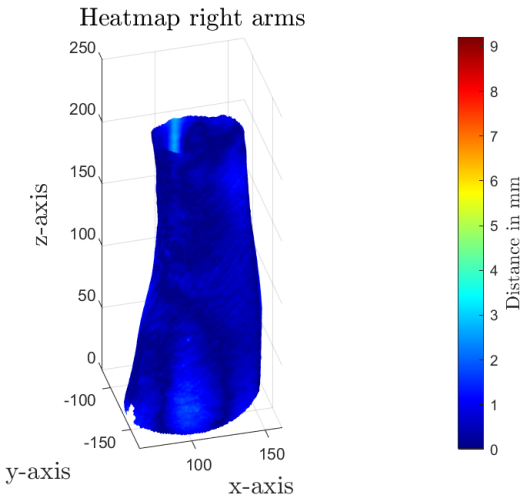

(a) Heatmap of the two scans of the right forearm.

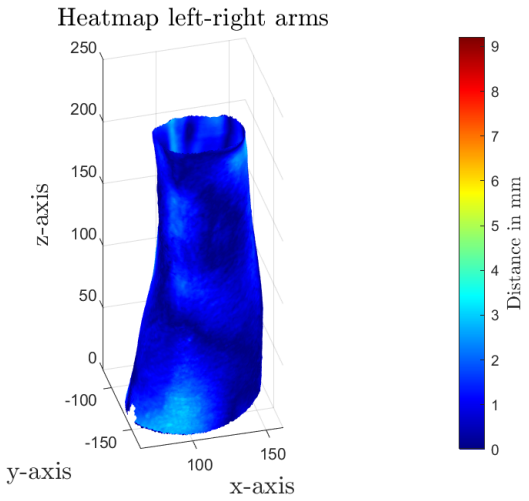

(b) Heatmap of the right and left forearm.

Figure B.8: Heatmaps of the forearm from participant 8.

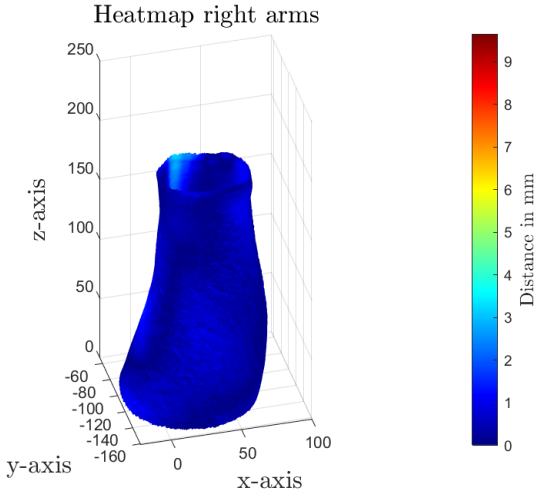

(a) Heatmap of the two scans of the right forearm.

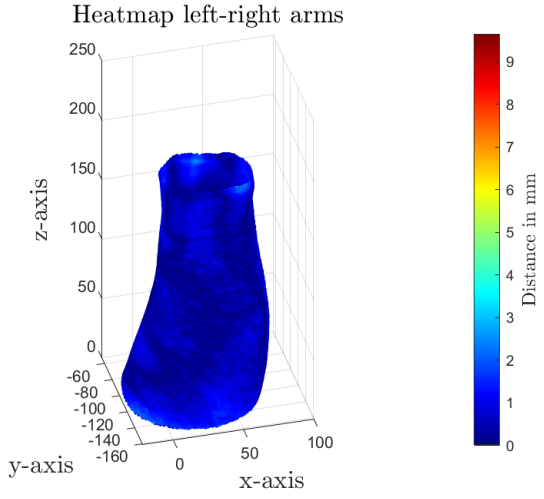

(b) Heatmap of the right and left forearm.

Figure B.9: Heatmaps of the forearm from participant 9.

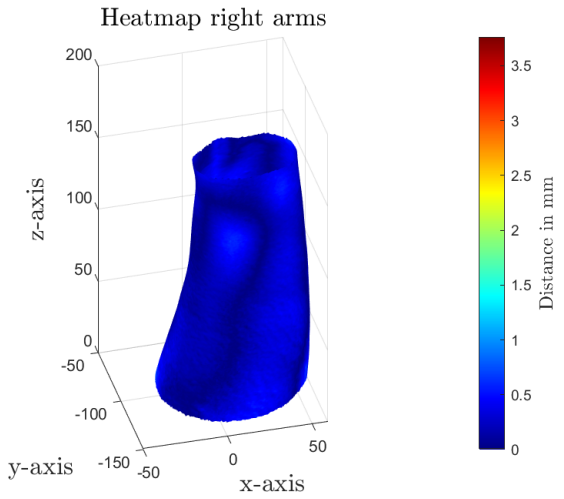

(a) Heatmap of the two scans of the right forearm.

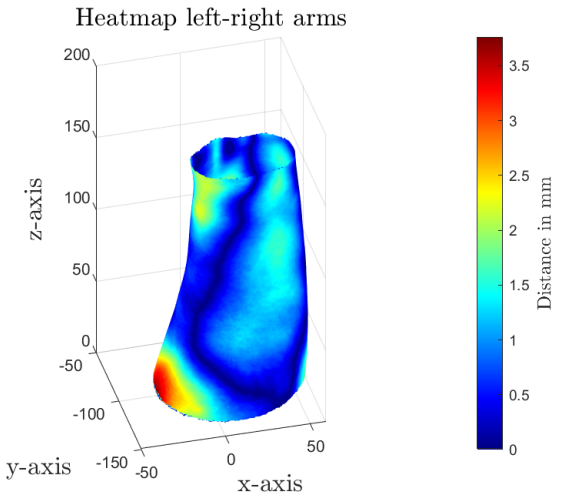

(b) Heatmap of the right and left forearm.

Figure B.10: Heatmaps of the forearm from participant 10.

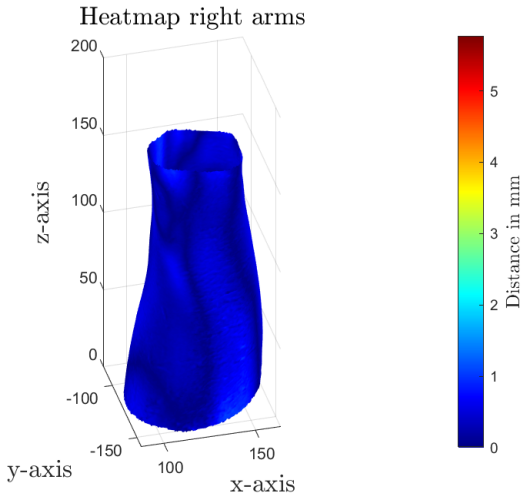

(a) Heatmap of the two scans of the right forearm.

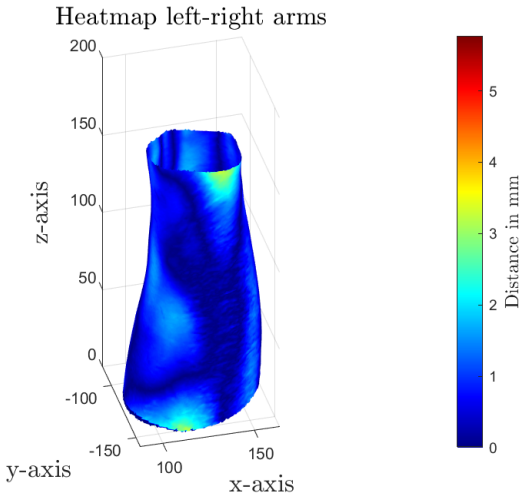

(b) Heatmap of the right and left forearm.

Figure B.11: Heatmaps of the forearm from participant 11.

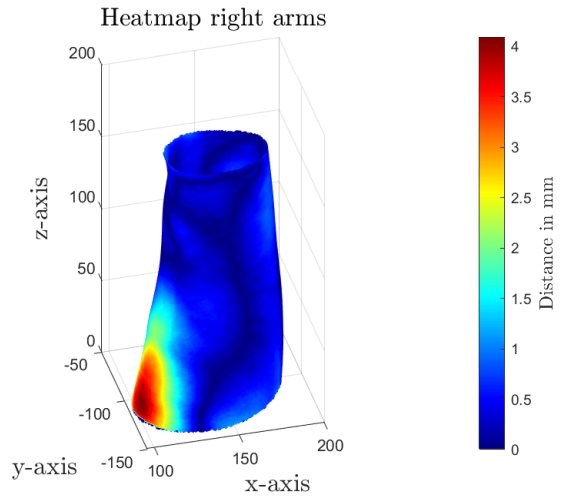

(a) Heatmap of the two scans of the right forearm.

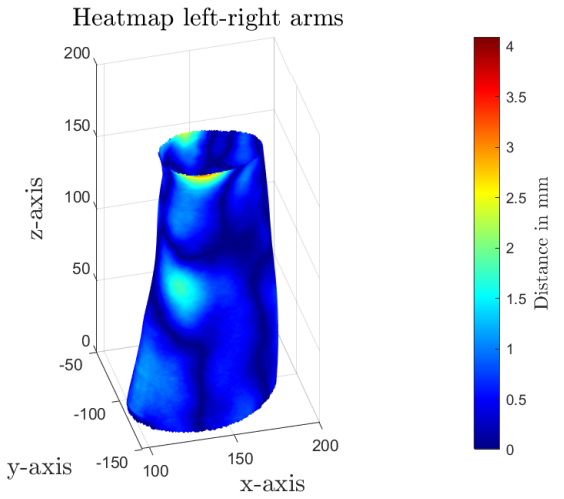

(b) Heatmap of the right and left forearm.

Figure B.12: Heatmaps of the forearm from participant 12.

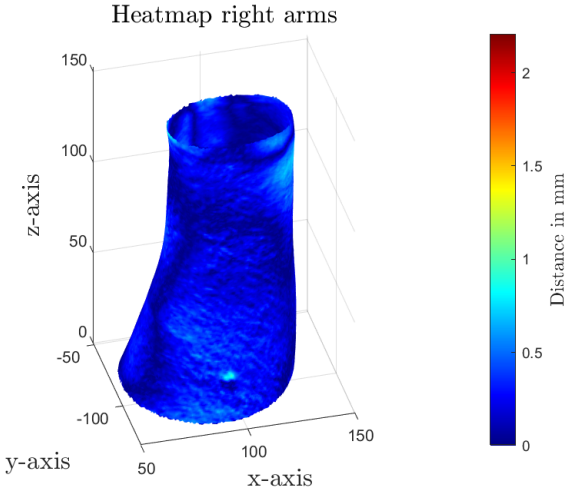

(a) Heatmap of the two scans of the right forearm.

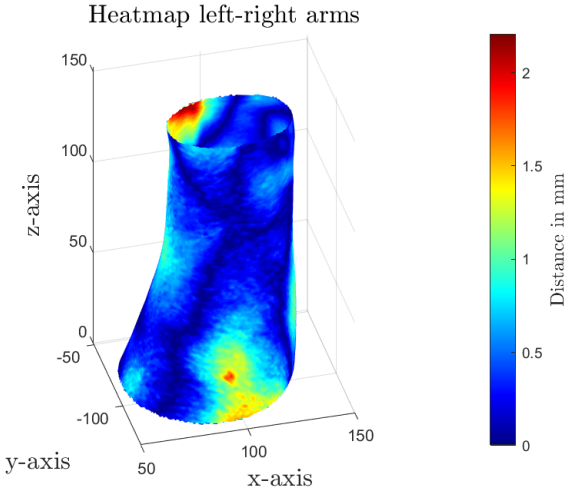

(b) Heatmap of the right and left forearm.

Figure B.13: Heatmaps of the forearm from participant 13.

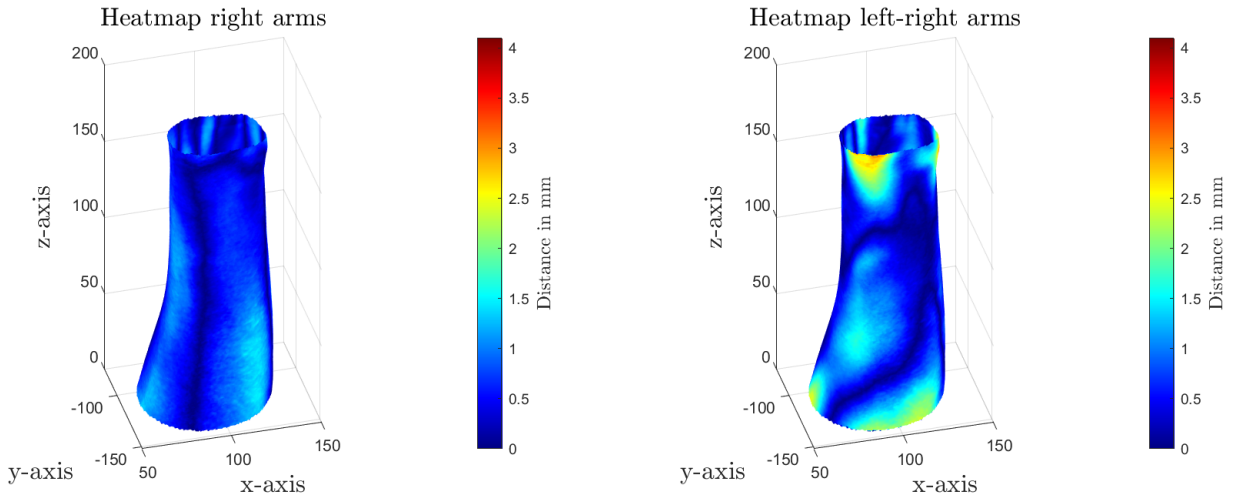

(a) Heatmap of the two scans of the right forearm.

(b) Heatmap of the right and left forearm.

Figure B.14: Heatmaps of the forearm from participant 14.

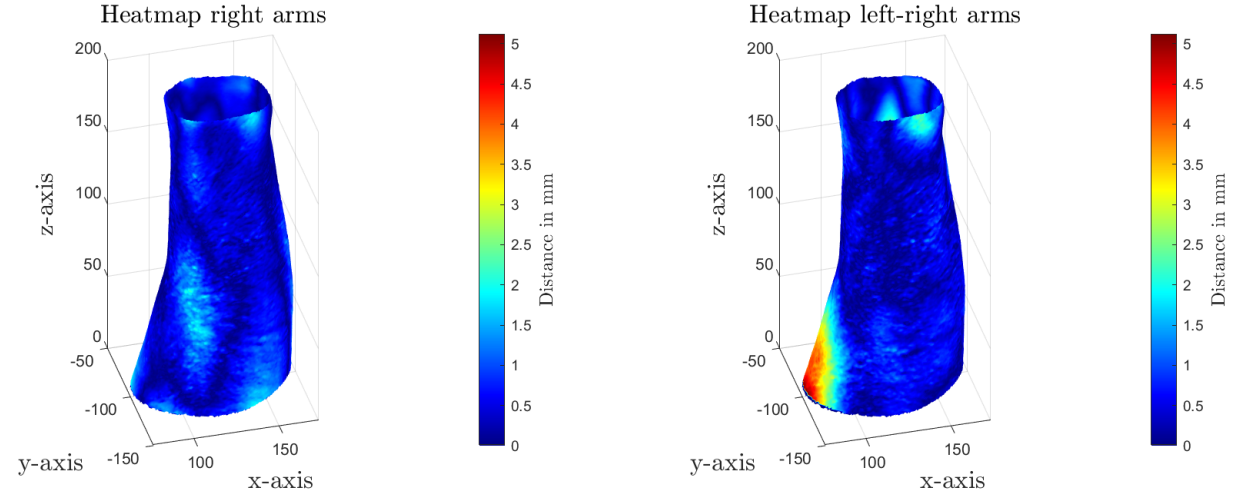

(a) Heatmap of the two scans of the right forearm.

(b) Heatmap of the right and left forearm.

Figure B.15: Heatmaps of the forearm from participant 15.